$$\text{III} \quad 1.0 \quad \begin{matrix} \text{2.8} & \text{2.5} \\ \text{3.2} & \text{2.2} \\ \text{3.6} & \\ \text{4.0} & \text{2.0} \end{matrix}$$

$$\text{III} \quad 1.1 \quad \quad \quad \text{1.8}$$

$$\text{III} \quad 1.25 \quad \text{1.4} \quad \text{1.6}$$

MICROCOPY RESOLUTION TEST CHART

NATIONAL BUREAU OF STANDARDS 1963 A

AD-A170 626

DNA-TR-85-282

OPTICAL PROPERTIES AND AERODYNAMIC DRAG CHARACTERISTICS OF BLOW-OFF PARTICULATES

E. J. Davis
R. Periasamy
University of Washington
1013 Northeast 40th Street
Seattle, WA 98195

DTIC
ELECT
S
AUG 0 6 1986
D
D

23 August 1985

Technical Report

Prepared for
Director
DEFENSE NUCLEAR AGENCY
Washington, DC 20305-1000

DTIC FILE COPY

86 8 6 008

DISTRIBUTION LIST UPDATE

This mailer is provided to enable DNA to maintain current distribution lists for reports. We would appreciate your providing the requested information.

☐ Add the individual listed to your distribution list.

☐ Delete the cited organization/individual.

☐ Change of address.

NAME: _____

ORGANIZATION: _____

OLD ADDRESS	CURRENT ADDRESS
_____	_____
_____	_____
_____	_____

TELEPHONE NUMBER: ( ) _____

SUBJECT AREA(s) OF INTEREST:

_____	_____
_____	_____
_____	_____

DNA OR OTHER GOVERNMENT CONTRACT NUMBER: _____

CERTIFICATION OF NEED-TO-KNOW BY GOVERNMENT SPONSOR (if other than DNA):

SPONSORING ORGANIZATION: _____
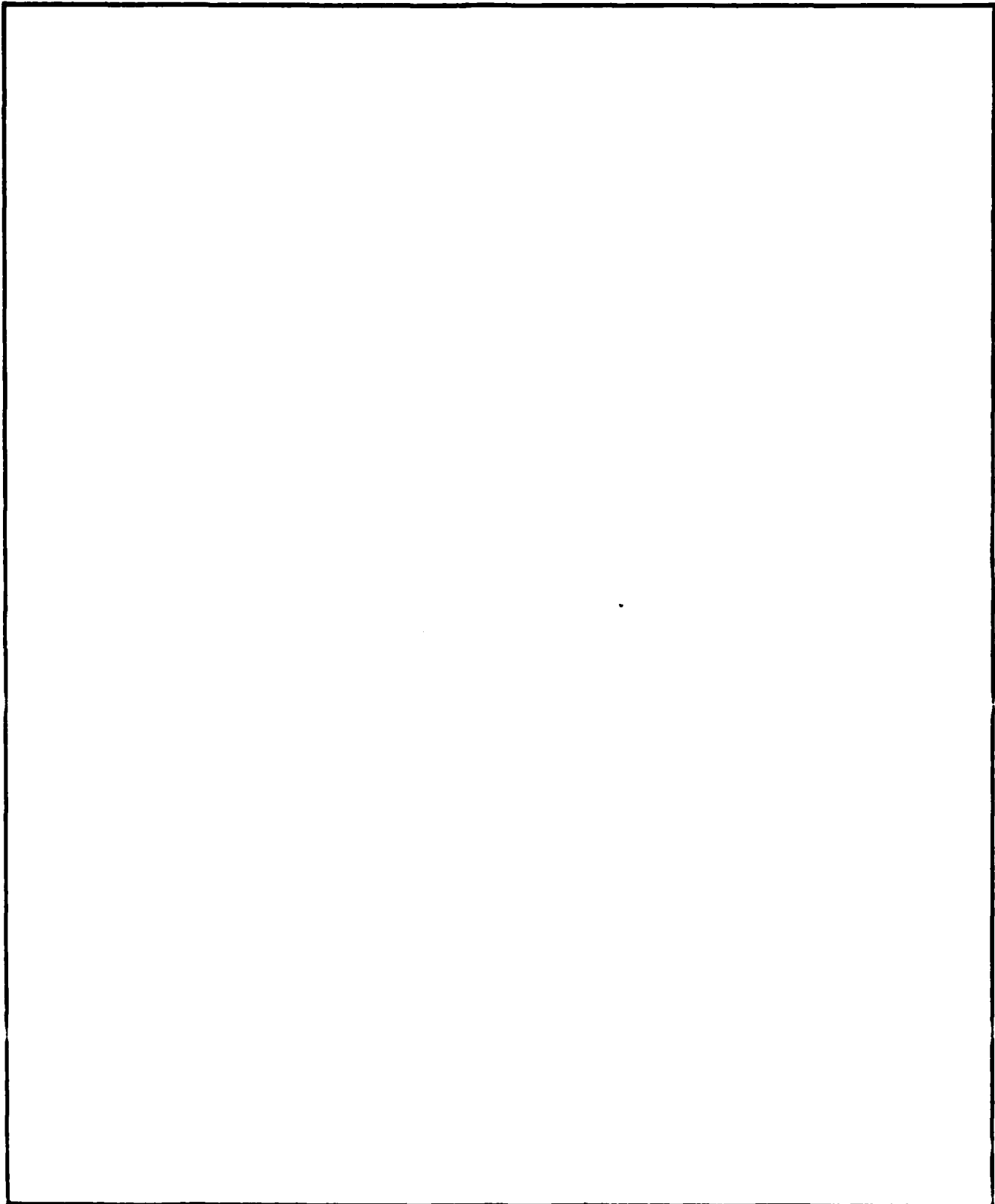
CONTRACTING OFFICER OR REPRESENTATIVE: _____

SIGNATURE: _____

UNCLASSIFIED
SECURITY CLASSIFICATION OF THIS PAGE

REPORT DOCUMENTATION PAGE	Form Approved OMB No 0704-0188 Exp Date Jun 30 1986

1a REPORT SECURITY CLASSIFICATION UNCLASSIFIED	1b RESTRICTIVE MARKINGS
2a SECURITY CLASSIFICATION AUTHORITY N/A since Unclassified	3 DISTRIBUTION AVAILABILITY OF REPORT Approved for public release; distribution is unlimited.
2b DECLASSIFICATION DOWNGRADING SCHEDULE N/A since Unclassified	

4 PERFORMING ORGANIZATION REPORT NUMBER(S) UW Project 62-9025	5 MONITORING ORGANIZATION REPORT NUMBER(S) DNA-TR-85-282

6a NAME OF PERFORMING ORGANIZATION University of Washington	6b OFFICE SYMBOL (If applicable)	7a NAME OF MONITORING ORGANIZATION Director Defense Nuclear Agency

6c ADDRESS (City, State, and ZIP Code) 1013 Northeast 40th Street Seattle, WA 98195	7b ADDRESS (City, State, and ZIP Code) Washington, DC 20305-1000

8a NAME OF FUNDING SPONSORING ORGANIZATION	8b OFFICE SYMBOL (If applicable)	9 PROCUREMENT INSTRUMENT IDENTIFICATION NUMBER DNA 001-84-C-0293

8c ADDRESS (City, State and ZIP Code)	10 SOURCE OF FUNDING NUMBERS

	PROGRAM ELEMENT NO	PROJECT NO	TASK NO	WORK UNIT ACCESSION NO
	62715H	Q93QMXS	G	DH251260

11 TITLE (Include Security Classification)

OPTICAL PROPERTIES AND AERODYNAMIC DRAG CHARACTERISTICS OF BLOW-OFF PARTICULATES

12 PERSONAL AUTHOR(S)
Davis, E.J. and Periasamy, R.

13a TYPE OF REPORT Technical Report	13b TIME COVERED FROM 840615 TO 850731	14 DATE OF REPORT (Year, Month, Day) 850823	15 PAGE COUNT 70

16 SUPPLEMENTARY NOTATION
This work was sponsored by the Defense Nuclear Agency under RDT&E RMSS Code X341084469 Q93QMXSG00014 H2590D.

17 COSATI CODES			18 SUBJECT TERMS (Continue on reverse if necessary and identify by block number)
FIELD	GROUP	SUB-GROUP	Aerosols Aerodynamic Drag Complex Refractive Index
20	6		Albedo Atmospheric Dust Optical Properties
19	4		Dust Thermal Dust Lights-Scattering

19 ABSTRACT Continue on reverse if necessary and identify by block number)

The results of the third and last phase of baseline studies on the electromagnetic scattering properties of the dust particles generated in simulated nuclear explosions and the aerodynamic drag characteristics of the particles are presented. Using techniques and equipment developed by the Principal Investigator, the complex refractive indices and particle sizes were measured by light-scattering in the visible range of the electromagnetic spectrum. It was not possible to extend the measurements into the ultraviolet region with the available equipment. Single particle albedos were determined from the light-scattering results. A new technique was developed and applied to measure the drag force on single particles suspended in a laminar gas jet, and results are reported for the ratio of the drag force to the particle weight as a function of the particle Reynolds number. It is shown that the properties are consistent with data for bulk silicates and that the particles are sufficiently near-spherical to use well-established results for spheres in drag force computations.

20 DISTRIBUTION AVAILABILITY OF ABSTRACT ☐ UNCLASSIFIED UNLIMITED ☒ SAME AS RPT ☐ DTIC USERS	21 ABSTRACT SECURITY CLASSIFICATION UNCLASSIFIED
22a NAME OF RESPONSIBLE INDIVIDUAL Betty L. Fox	22b TELEPHONE (Include Area Code) (202) 325-7042	22c OFFICE SYMBOL

DD FORM 1473, 84 MAR

SUMMARY

This document is a final report on the measurements of the light-scattering properties and aerodynamic drag characteristics of blow-off particles generated in simulated thermonuclear blasts. The "thermal dust particles" examined were generated in experiments performed by Science Applications Inc. (SAI) under a separate DNA contract, using a solar furnace in Odeillo, France. The samples obtained from SAI consisted of filters, wall wipings and loose dust taken from various locations in the solar furnace, and they correspond to various soil samples placed in the furnace for the tests.

The data contained herein include particle size and shape, complex refractive indices, single particle albedo results and aerodynamic drag forces as a function of gas velocity. A new technique was developed and applied for the first time here for the direct measurement of aerodynamic drag forces on micron-size particles.

The optical properties of blow-off particulate matter in the aerosol size range were found to be similar to the bulk properties of mixed silicates with the measured real components of the complex refractive indices in the range 1.391 to 1.647. The wavelengths used in the three phases of the research were in the range 454.5 nm to 632.8 nm. In this range the refractive indices were so nearly constant that no dispersion relation could be calculated from the data to correlate the refractive index as a function of wavelength. The imaginary components of the complex refractive indices were found to be near zero within the limits of experimental error, indicating that little absorption of the light occurred in the visible region of the spectrum of electromagnetic radiation. Single particle albedos were determined to be approximately unity, ranging from 0.68 to 0.99 based on the measured complex refractive indices.

Although many particles had irregular shapes, the drag forces on them were approximately the same as for spheres. With few exceptions the aerodynamic drag characteristics of the particles were found to satisfy the Stokes relation for the drag force, using the aerodynamic radius as the equivalent radius of the sphere.

Accesion For		
NTIS CRA&I	☑	
DTIC TAB	☐	
Unannounced	☐	
Justification		
By		
Distribution /		
Availability Codes		
Dist	Avail and / or Special	
A-1		

iii

PREFACE

The work reported here represents the third and last phase of baseline studies on the optical properties and aerodynamic drag characteristics of blow-off particles. The results of Phase I, which involved the development of instrumentation, measurement techniques and computer software, were summarized in Report No. DNA 6274F, dated 18 April 1983. Phase I was supported under DNA Contract No. DNA 001-80-C-0213. The work on Phase I was performed at the Institute of Paper Chemistry in Appleton, Wisconsin under a subcontract with the University of New Mexico. Phase II, which involved light-scattering measurements, was summarized in a report on DNA Contract No. DNA 001-84-C-0224 dated 29 February 1984. Part of the work on Phase II was performed at the Institute of Paper Chemistry, and the work was completed at the University of Washington under a subcontract with the Institute of Paper Chemistry.

CONVERSION TABLE

To convert from	to	multiply by
Å, Angstrom units	m, meters	10^{-10}
µm, micrometers	m, meters	10^{-6}
nm, nanometers	m, meters	10^{-9}

TABLE OF CONTENTS

LIST OF ILLUSTRATIONS

LIST OF ILLUSTRATIONS (CONCLUDED)

LIST OF TABLES

SECTION 1
OBJECTIVES

The objectives of this research were to measure the aerodynamic drag characteristics and light-scattering properties of dust particles generated thermally in a solar furnace. The following properties were measured and are reported here:

1. The aerodynamic drag force as a function of Reynolds number.
2. The aerodynamic diameter.
3. The particle mobility (ratio of velocity to drag force)
4. The light-scattering phase function (scattering intensity versus angle) as
   a function of wavelength of the incident radiation.
5. The complex refractive index.
6. The single particle albedo.
7. The particle size.

1.1 BACKGROUND

1.1.1 Light Scattering Theory

The scattering of electromagnetic radiation by a spherical dielectric particle is described by Mie theory [1] in terms of the complex refractive index, $m = m_1 - im_2$, the dimensionless light-scattering size, $\alpha = 2\pi a/\lambda$, and the angular positions of the detector, ϕ and θ, where ϕ and θ, are measured as indicated in Figure 1. In the experiments described herein the detector is rotated only in the x-y plane, so $\phi = \pi/2$, and ϕ will not appear explicitly.
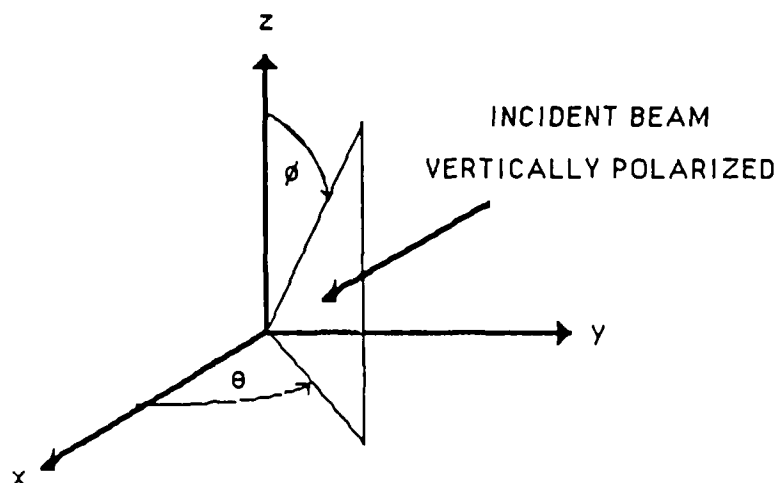
Figure 1. The light-scattering coordinates.

The scattered intensity, I_s, is given by the following equation

$$I_s = \left| \sum_{n=1}^{\infty} \frac{2n+1}{n(n+1)} [a_n \Pi_n(\cos\theta) + b_n \tau_n(\cos\theta)] \right|^2, \qquad (1)$$

where the scattering coefficients, a_n and b_n are given by

$$a_n = \frac{\psi_n'(m\alpha)\psi_n(\alpha) - m\psi_n(m\alpha)\psi_n'(\alpha)}{\psi_n'(m\alpha)\xi_n(\alpha) - m\psi_n(m\alpha)\xi_n'(\alpha)} \qquad (2)$$

and

$$b_n = \frac{m\psi_n'(m\alpha)\psi_n(\alpha) - \psi_n(m\alpha)\psi_n'(\alpha)}{m\psi_n(m\alpha)\xi_n(\alpha) - \psi_n(m\alpha)\xi_n(\alpha)}. \qquad (3)$$

---

[1]   Mie, G. *Ann. Phys.* (Leipzig) **25**, 377 (1908).

The function, ψ_n, is defined in terms of the spherical Bessel function, j_n, by the equation

$$\psi_n(\alpha) = \alpha j_n(\alpha), \tag{4}$$

and the function, ζ_n, is given in terms of ψ_n and the Neuman function, $N_n(\alpha)$, as follows

$$\zeta_n(\alpha) = \psi_n(\alpha) + i N_n(\alpha). \tag{5}$$

Primes indicate differentiation of the functions with respect to their appropriate arguments. The functions $\Pi_n(\cos\theta)$ and $\tau_n(\cos\theta)$ are written in terms of Legendre functions, $P_n^{(1)}$, as follows

$$\Pi_n(\cos\theta) = P_n^{(1)}(\cos\theta)/\sin\theta, \tag{6}$$

and

$$\tau_n(\cos\theta) = \frac{d}{d\theta}[P_n^{(1)}(\cos\theta)]. \tag{7}$$

In general, the scattering efficiency factor, Q_{sca}, depends on the orientation of the particle and on the state of polarization of the incident light, but for a spherical particle Q_{sca} is independent of both and is given by

$$Q_{sca} = \frac{2}{\alpha^2} \sum_{n=1}^{\infty} (2n+1)(|a_n|^2 + |b_n|^2). \tag{8}$$

The total extinction efficiency factor, Q_{ext}, which consists of the efficiency of scattering plus the absorption efficiency, can be expressed in terms of the Mie scattering coefficients as

$$Q_{ext} = \frac{2}{\alpha^2} \sum_{n=1}^{\infty} (2n+1)\text{Re}(a_n + b_n), \tag{9}$$

where Re refers to the real part of the argument.

Finally, the albedo, A, of the single particle is given by

$$A = Q_{sca}/Q_{ext}. \tag{10}$$

The albedo is unity for a particle which absorbs none of the electromagnetic energy, and it is zero for a totally absorbing sphere.

For a nonspherical particle the equations governing the light scattering are not tractable, but many of the dust particles encountered in this research had reached temperatures high enough to melt and, thus, were spherical. In this case the particle size and its complex refractive index were obtained by comparing theoretical phase functions (I_s as a function of θ) computed using Equation (1) with experimental data for the scattering intensity as a function of angle in the horizontal plane.

1.1.2 Principles of the Electrodynamic Balance

To obtain the light-scattering data a charged dust particle was suspended in a vertically polarized laser beam by means of superposed ac and dc electrical fields. The combination light-scattering photometer and electrodynamic balance developed by Davis and Ray[2] was used for the most of the experiments, but some experiments were performed with a new device of improved design. The former apparatus and a schematic diagram of the circuitry are shown in Figure 2.
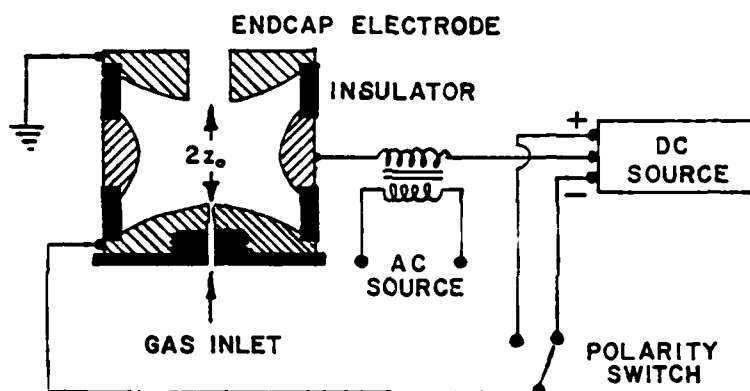
Figure 2. The electrodynamic balance and associated circuitry.

An exploded view of the light-scattering chamber is shown in Figure 3. The upper and lower endcap electrodes and the ring electrode have inner surfaces of hyperbolic shape, and the ring electrode has a window inserted at its midplane which covers the angle range $5° < \theta < 175°$. A traversing photomultiplier tube (PMT), driven by a stepping motor, was used to measure the intensity of the scattered light as it was rotated around the light-scattering cell. The output of the PMT and the voltage applied to the stepping motor were recorded on an X-Y plotter and/or stored on floppy disks using a MINC-23 digital computer (Digital Equipment Corp.) to provide the record of intensity versus angle needed for comparison with Mie theory.

---

2   Davis, E. J., and Ray, A.K., *J. Colloid Surface Sci.* **75**, 566 (1980).
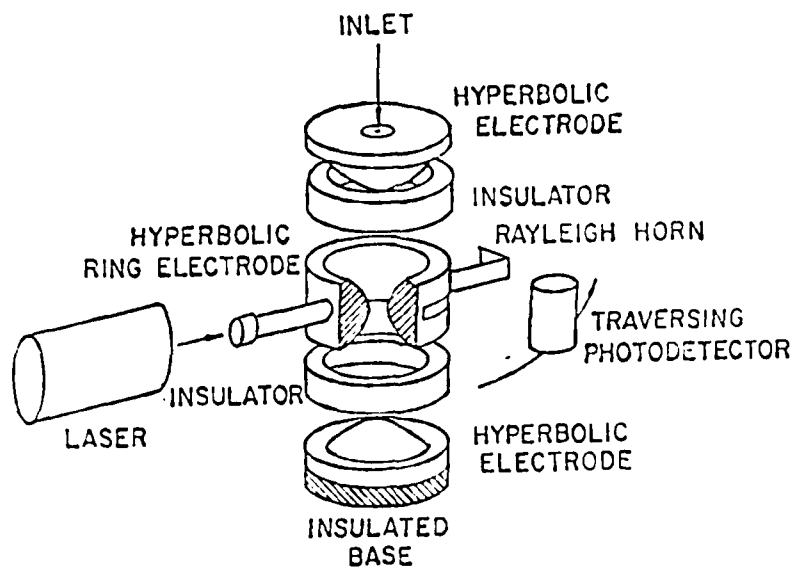
Figure 3. An exploded view of the electrodynamic balance.

The function of the ac field generated by the ring electrode is to focus the charged particle near the center of the balance chamber, and the dc field is used to balance the gravitational force. In the absence of a dc field the particle oscillates near the center of the balance, and when the vertical component (z-component) of the dc field satisfies the following force balance the particle remains stationary at the null point of the chamber:

$$qE_{dc,z} - mg = 0, \tag{11}$$

where q is the charge on the particle, $E_{dc,z}$ is the vertical component of the dc field, m is the particle mass, and g is the gravitational acceleration constant. The dc field is given by

$$E_{dc,z} = C_0 V_0 / 2z_0, \tag{12}$$

where V_0 is the voltage applied to the lower endcap electrode, C_0 is a geometrical constant of the balance, and $2z_0$ is the minimum distance between the upper and lower electrodes.

Thus, in the absence of other forces (such as aerodynamic drag and photophoretic forces) the voltage, V_0, required to suspend the particle in the laser beam passing through the center of the balance is

$$V_0 = 2mgz_0 / qC_0. \tag{13}$$

3

1.1.3 Drag Force Measurement

If a uniform flow of gas is passed upward through the balance chamber, the suspended particle will experience a drag force which depends on the gas velocity and the particle shape. Dahneke [3] reviewed the literature on the aerodynamic drag on small (low Reynolds numbers) nonspherical bodies, and for creeping flow shape and slip correction factors can be introduced to give the generalized equation,

$$F_d = K_o L_c \mu U_\infty / (1+f), \qquad (14)$$

where F_d is the aerodynamic drag force, K_o is the resistance constant, μ is the gas viscosity, L_c is the characteristic dimension of the particle, U_∞ is the gas velocity in the mainstream of the flow, and f is the slip correction factor. The slip correction factor allows for deviations from continuum theory which occur when the gas pressure is low. At normal atmospheric pressure f may be taken to be zero, and we shall assume it to be zero in this report.

For spherical particles in the continuum regime Equation (14) reduces to Stokes' equation,

$$F_d = 6\pi a \mu U_\infty, \qquad (15)$$

where a is the sphere radius. Equation (15) is valid for Re < 1, where the Reynolds number is defined by $Re = 2aU_\infty/\upsilon$, and υ is the kinematic viscosity of the gas. For somewhat higher Reynolds numbers Oseen's solution [4] can be used, which is

$$F_d = 6\pi a \mu U_\infty (1 + 3Re/16 + 19Re^2/2560 + \cdots\cdots). \qquad (16)$$

Dahneke reported shape correction factors for various bodies with well-defined shapes such as rods, disks, oblate spheroids and prolate spheroids, but for aerosol particles of irregular shape experimental data are generally unavailable.

To obtain aerodynamic drag data for the blow-off dust particles the electrodynamic balance was modified to provide a flow of metered nitrogen upward along the vertical axis of the chamber. This was accomplished by drilling a small hole (1.5 mm diameter) in the bottom electrode to permit a laminar jet of gas to enter the chamber. The aerodynamic drag force, then, acted in the upward direction in opposition to gravity. Thus, the dc electrical field needed to balance the particle was altered by the flow and can be used to determine the drag force. When the jet velocity is just large enough to pro-duce a drag force equal to the gravitational force, no dc field is required to balance the particle, and for

---

3   Dahneke, B. E., *J. Aerosol Sci.* **4**, 139 (1973).

4   Oseen, C., *Neure Methoden und Ergebnisse in der Hydrohynamik*, Akademische Verlag, Leipzig, German. 1927.

3

low Reynolds numbers the critical velocity, U_c, corresponding to this force balance must satisfy the equation,

$$K_0 L_c \mu U_c = mg. \tag{17}$$

In general, the force balance on the particle is given by

$$C_0 q V_{dc}/2z_0 + F_d - mg = 0. \tag{18}$$

It is convenient to write Equation (18) in an alternate form by dividing the equation by mg and using Equation (13) to eliminate the charge-to-mass ratio, q/m. The result can be written in the form

$$F_d/mg = 1 - V_{dc}/V_0, \tag{19}$$

where V_{dc} and V_0 are the dc voltages required to suspend the particle with and without gas flow, respectively. Since V_{dc} is a function of the gas flow rate, the drag characteristics of a particle can be determined over a fairly wide range of flow rates by simply measuring the voltage required to suspend the particle with no flow through the chamber, then with various flow rates up to the limit of the stability of the particle in the balance. We shall report the drag force to weight ratio, F_d/mg, for the experiments performed in this research.

1.1.4 Calibration of the Electrodynamic Balance

Two calibrations were involved with the apparatus. The first was the determination of the geometrical constant, C_0, appearing in the force balance equations. The second calibration was that of the jet velocity as a function of the metered gas flow rate.

The value of C_0 was determined by the method outlined by Davis [5] based on the stability characteristics of the electrodynamic balance. The ac field which provides the focusing of the particle causes the particle to oscillate when the dc field does not balance gravity, and the oscillation is damped by the viscous drag of the surrounding gas. This is true provided that the ac field strength is

---

5   Davis, E. J., Langmuir 1, 379 (1985).

not too large to overcome viscous damping. At lower frequencies and higher amplitudes of the ac voltage the particle becomes unstable and cannot be maintained in a stationary state at the center of the balance. By measuring the ac voltage above which the particle cannot be stably balanced (the marginal stability state) and by using the theoretical results of the stability theory of the balance, the geometrical constant was found to be given by $C_0 = 0.471$ with a standard deviation of 0.054 and a mean deviation of 9.1% based on 20 experiments performed with dibutyl phthalate droplets of various diameters.

The droplet diameter was determined by light-scattering measurements, and the droplet mass calculated from the droplet diameter and the known density of the liquid. The experiments were performed by capturing a droplet in the balance using an ac field lower than the marginal stability state. The dc voltage required for suspension was recorded, and light-scattering data were obtained. Then the ac voltage was increased until sudden, large-amplitude oscillations were observed in the microscope attached to the ring electrode. By comparison of the measured marginal stability state with the theoretical predictions of Davis, the geometrical constant was determined.

The jet velocity was calibrated by suspending spherical particles and droplets, whose sizes were measured by light-scattering, at various flow rates. The critical volumetric flow rate, Q_c, required to balance gravity and the no-flow voltage, V_0, were measured for each droplet. The critical velocity, U_c, corresponding to that flow rate was calculated using the equation,

$$6\pi a\mu U_c(1 + 3Re_c/16 + 19Re_c^2/2560) - mg = 0, \tag{20}$$

where the droplet mass is obtained from the droplet radius by $m = 4\pi a^3\rho_L/3$, where ρ_L is the density of the liquid. For $Re_c < 1$ this reduces to

$$U_c = 2\rho_L a^2 g/9\mu. \tag{21}$$

Equations (20) and (21) are also the basis for determining the aerodynamic radius from measured values of the critical flow rate, for once the jet velocity was calibrated the same procedure was used to determine the radius.

Figure 4 shows the calibration results for nitrogen at room temperature. At higher flow rates the jet velocity is approximately proportional to Q^2, which is consistent with laminar jet theory [6]. For a cir-

---

[6]   Schlichting, H., *Boundary-Layer Theory*, 6th edition, McGraw-Hill, 1968.

cular laminar jet, if the momentum of the jet is conserved, we may write

$$J = 2\pi\rho \int_0^\infty u^2 r\,dr = \text{constant}, \qquad (22)$$

where J is the flux of momentum, ρ is the fluid density, u is the local jet velocity, and r is the radial position. The velocity distribution for the laminar jet is given by

$$u = \frac{3}{8\pi} \frac{K}{\nu z} \frac{1}{(1 + \xi^2/4)^2} , \qquad (23)$$

where K is the kinetic momentum of the jet ($K = J/\rho$), z is the distance from the orifice, and ξ is defined by

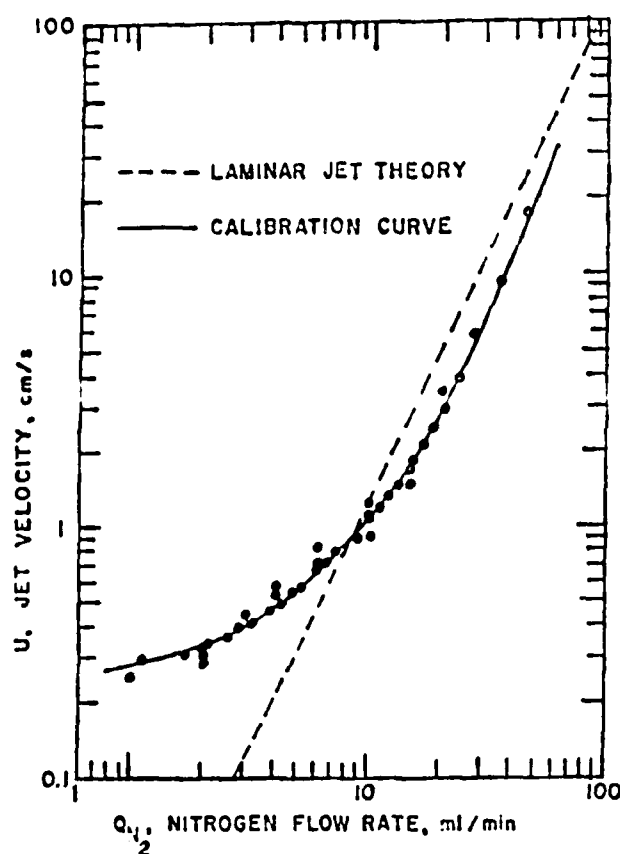$$\xi = \left(\frac{3K}{16\pi} \right)^{1/2} \frac{r}{\nu z} . \qquad (24)$$

Figure 4. The calibration of the jet velocity for drag measurement.

Now the kinetic momentum can be approximated by the momentum of the gas leaving the hole in the

bottom electrode. If the flow in that tube is Poiseuille flow, its kinematic momentum is given by

$$K = 16Q^2/3\pi d_o^2, \qquad (25)$$

where Q is the volumetric flow rate of gas and d_o is the diameter of the hole. Thus, using Equation (25) in Equation (23) and evaluating the velocity at the center of the balance (r = 0 and z = z_o), we obtain

$$u_o = 2Q^2/\pi^2 d_o^2 \upsilon z_o. \qquad (26)$$

Equation (26) is also plotted on Figure 4. The experimental data for high flow rates fall below but are parallel the theoretical velocities predicted using Equation (26). At low flow rates the velocities diverge significantly from the results predicted for a free laminar jet, for the jet velocities are greater than predicted values. This is a result of jet expansion and entrainment of surrounding gas by the jet, as indicated in Figure 5a and 5b. Figure 5a shows the jet velocity profiles for two vertical planes predicted using Equation (23) for the free jet for a nitrogen flow rate of 10 ml/min, and Figure 5b shows profiles for a flow rate of 30 ml/min. At the lower flow rate the jet expands to interact with the walls of the container before it reaches the midplane, so the jet cannot be considered to be a free jet. At the higher flow rate there is less interaction with the bounding surfaces, and the jet approaches free-jet behavior.
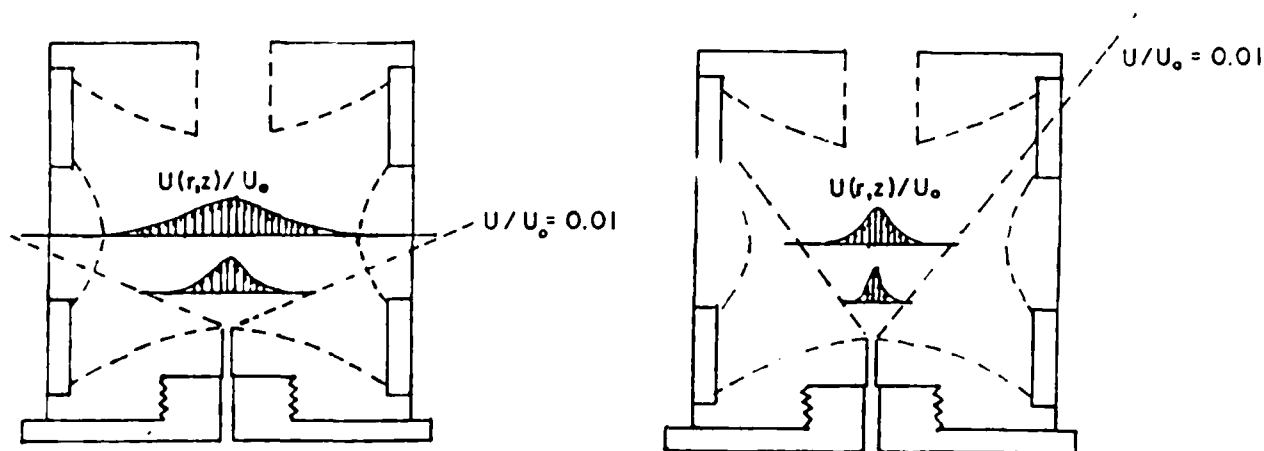

Figure 5 a,b. Calculated jet velocity profiles for a nitrogen flow rate of 10 ml/min and 30 ml/mi, respectively

SECTION 2
EXPERIMENTAL PROCEDURES AND DATA ANALYSIS

2.1   EXPERIMENTAL TECHNIQUES

2.1.1 Particle Injection

Liquid droplets and the blow-off dust particles were charged and injected into the balance in the same manner.   A small liquid drop was partly formed at the tip of a stainless steel capillary, and a dc voltage of 2 to 5 kV was suddenly applied to the capillary from a high voltage supply.   The high charge density on the liquid surface reduced the effective surface tension to zero, causing the droplet to fall into the balance.   With the ac voltage preset to approximately 1000 V rms, the droplet was trapped. The dc voltage was then adjusted to stop the droplet oscillation, as observed through a 70X microscope attached to the balance.   The droplet was suspended at the null point through which passed a vertically polarized laser beam.   For most of the experiments a tunable dye laser (Coherent Inc. Model CR-599), pumped by an argon-ion laser (Coherent Inc. Model Innova 90-5), was the light source, but in November 1984 the pump laser failed, and the laser system was replaced by an available Spectra Physics laser operating at a fixed wavelength of 632.8 nm.   Rhodamine 6G was the dye used in the dye laser, and this provided wavelengths in the range 575-650 nm.   Most of the light-scattering data reported herein were obtained at 605 nm, and data in the report on Phase II of the program were for wavelengths of 457.6, 488.0 and 514.5 nm.   Due to failure of the pump laser it was not possible to make measurements in the near-ultra violet region of the spectrum.

When blow-off particles were studied, the particles were washed from the filters or wiping material supplied by SAI, and a droplet consisting of a dilute suspension of the particles was injected into the balance.   The water evaporated within a few seconds, leaving the charged particle in the laser beam.

2.1.2 Light-Scattering Data Acquisition

Prior to capturing a particle the light-scattering data acquisition system was activated to record background intensities.   Background signals were also recorded at the end of a run. These data were used to correct the light-scattering data obtained with a suspended particle.

After a particle had been suspended in a dry gas stream for about two hours to remove all water from its surface the rotating photomultiplier tube was activated and the scattering intensities versus

11

angle were recorded on an X-Y plotter. Based on the plotted data, adjustments to the detector voltage or other desired corrections were made, and then the data were digitized and stored on floppy disks of a digital computer. The stored data were later replotted using a Hewlett-Packard printer/plotter (Model 7245B) connected to the computer.

Usually a forward scan (increasing ,) and a backward scan (decreasing ,) with the PMT were made and compared. If a particle was nonspherical, it was usually observed to "twinkle" in the microscope, and the forward and backward scans would not match because of particle rotation.

A representative experimental phase function for a blow-off dust particle is shown in Figure 6.
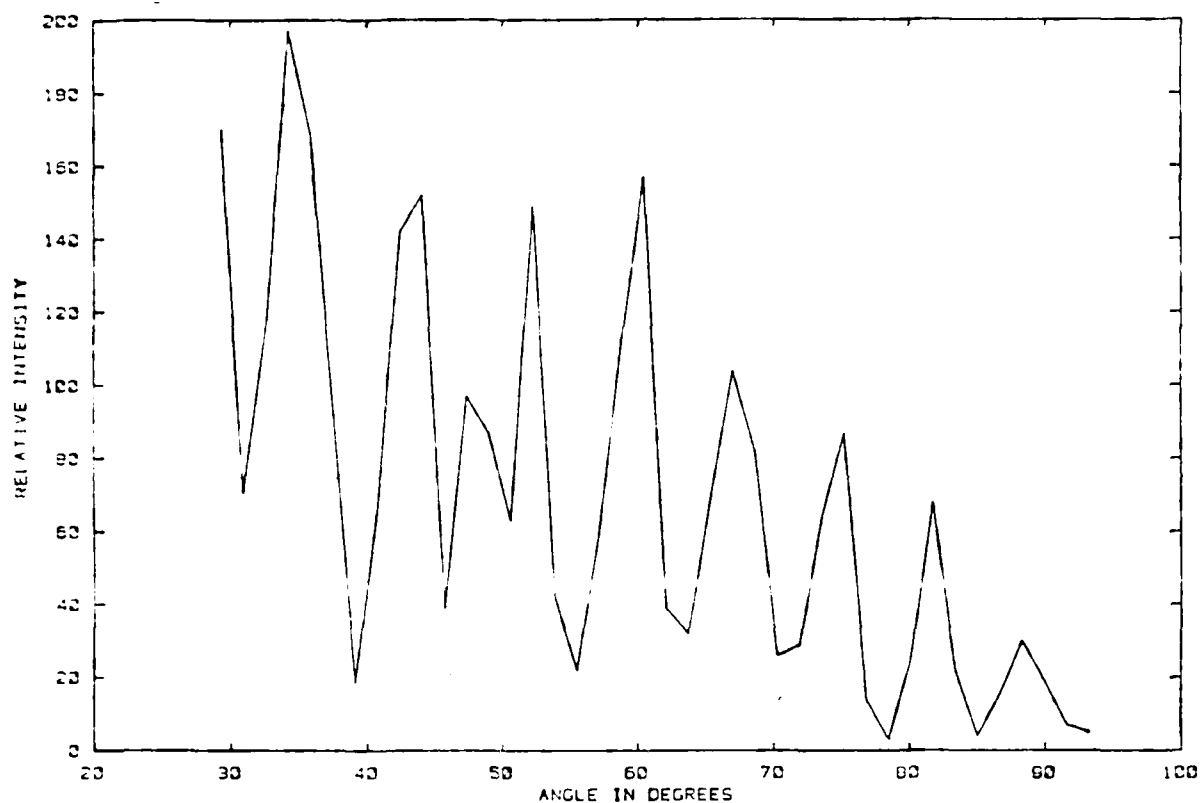

Figure 6. A typical phase function obtained for a blow-off dust particle.

2.1.3 Drag Force Data Acquisition

After the light-scattering data were o   ned, the gas flow rate was varied and the dc voltage was recorded as a function of flow rate. In many runs the flow rate was increased until the particle was blown from the balance. At higher flow rates a particle would begin to move off the centerline of the balance, and at yet higher flow rates it would be lost.

Typical data for dust particles are presented in Figure 7 as a plot of the dc voltage required for stable suspension versus the nitrogen flow rate. In this case the particles were positively charged, and the voltage decreased nonlinearly from some positive value, crossed the axis at the critical flow rate, Q_c, and continued to decrease as the flow rate was increased.
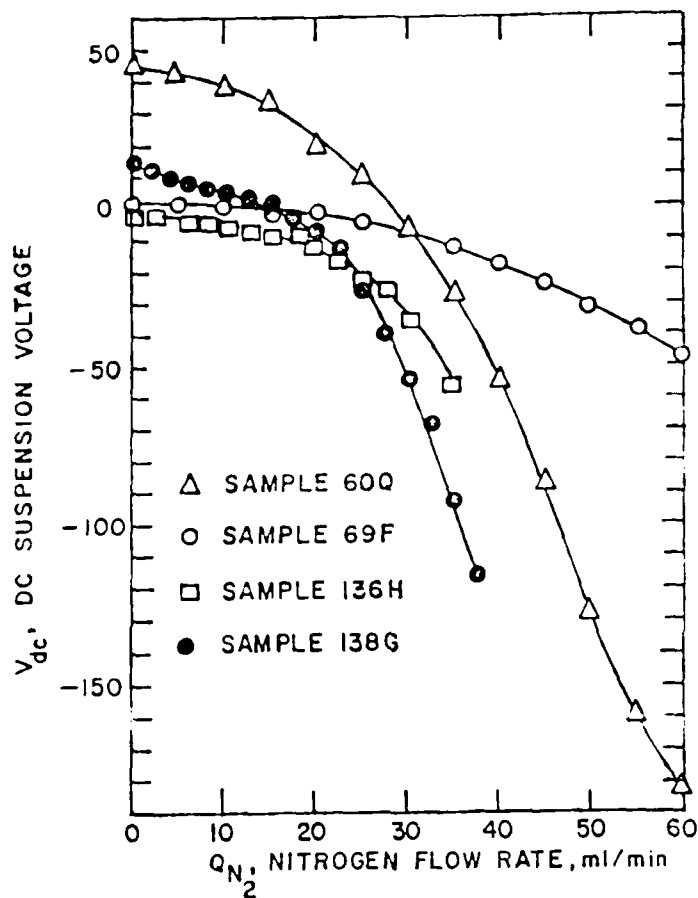

Figure 7. The dc suspension voltage as a function of nitrogen flow rate for representative blow-off dust particles.

The data from Figure 7 are replotted in terms of the drag force-to-weight ratio, F_d/mg, versus nitrogen velocity in Figure 8. For each particle the drag force is seen to be a linear function of velocity, which indicates that the flow was in the creeping flow regime. Note that for Sample 136H the ratio F_d/mg exceeded 110, and yet the drag force varied linearly with the jet velocity.
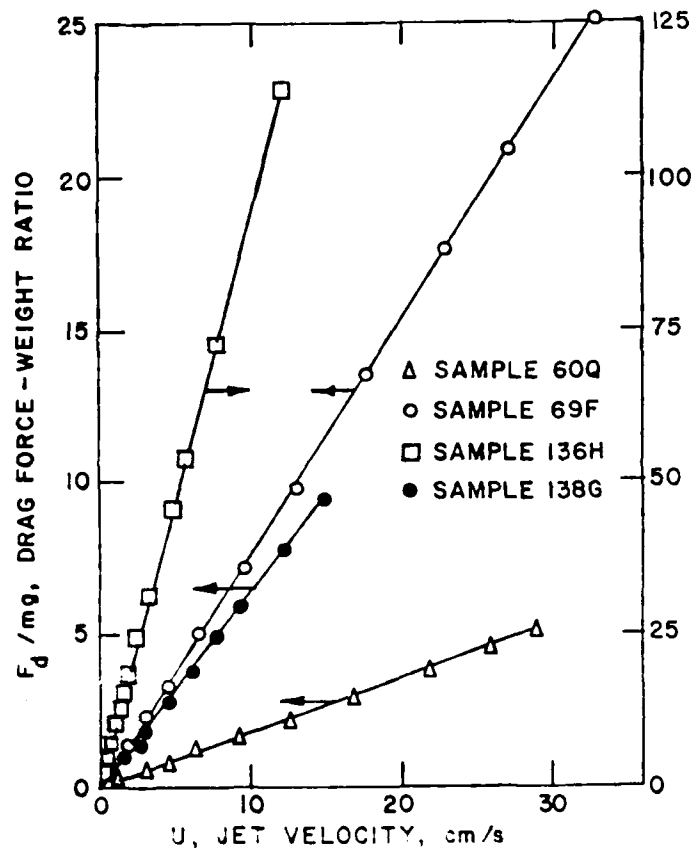
Figure 8. The drag force-to-weight ratio as a function of nitrogen velocity for the data of Figure 7.

An atypical set of data for three particles is shown in Figures 9 and 10. These particles were of irregular shape and show nonlinear drag force behavior. It appears that particle 60M underwent realignment as the gas velocity increased, for it is clear from Figure 10 that the slope of the curve of F_d/mg versus U changed significantly as the velocity increased. Sample 60P and, to a lesser extent, Sample 69K also showed systematic deviations from linearity. Particle 69K had an estimated aerodynamic radius of only 0.582 μm, which was one of the smaller particles examined, and the drag force-weight ratio reached 900 before the particle was lost.
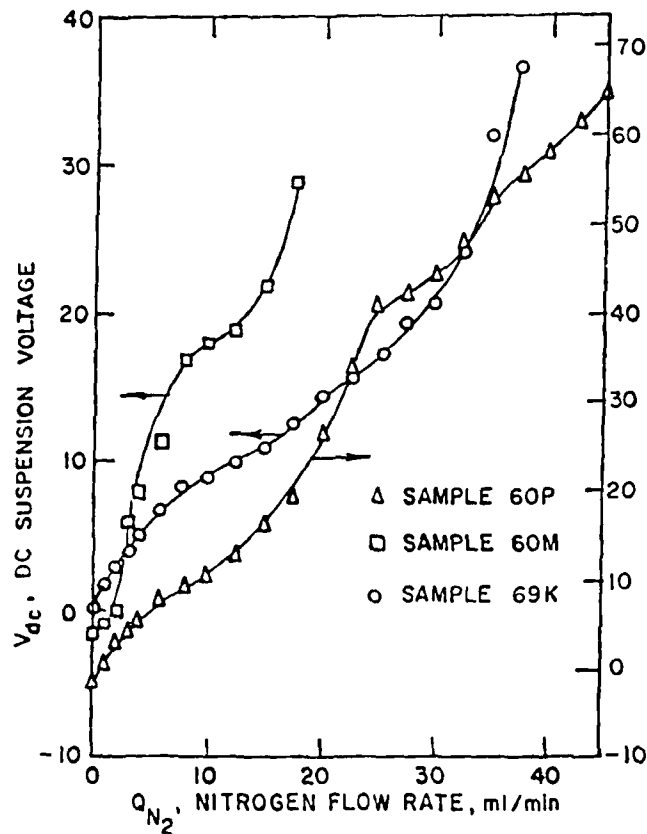
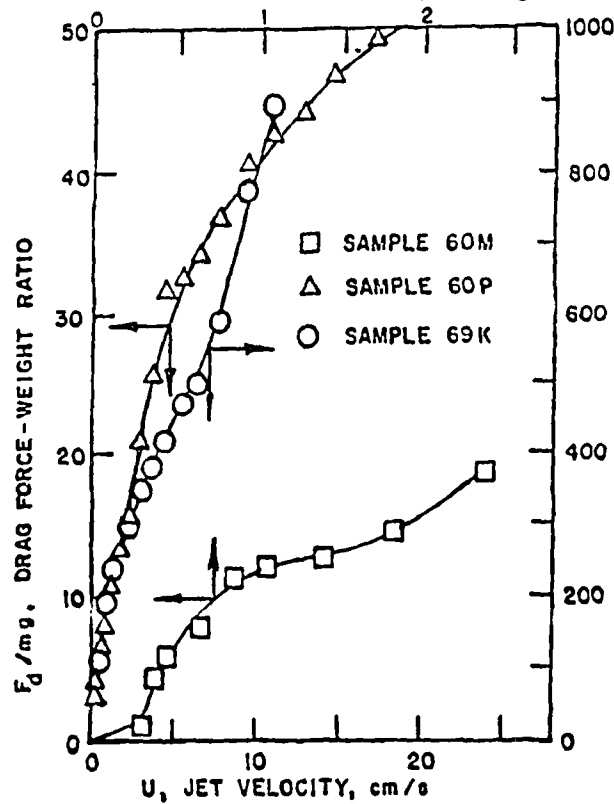Figure 9. Raw data for particles showing atypical drag characteristics.

Figure 10. Nonlinear drag characteristics of blow-off dust particles.

15

2.2 INTERPRETATION OF THE LIGHT-SCATTERING DATA

The analysis of the light-scattering phase functions follows that of Davis and Ravindran [7] who applied the Marquardt-Levenberg algorithm [8] to determine the complex refractive index and optical size from data by comparison with Mie theory.

Forty equally-spaced data points in the angle range 30° to 130° were selected, and the intensities, I_t, predicted from Mie theory for these angles were computed using trial values of the unknown parameters ($m = m_1 - im_2$, and α). The voltages from the photodetector circuit were converted to normalized intensities using the relation,

$$I_e(\theta_i) = \sigma[V(\theta_i) - V_b(\theta_{i_i})], \qquad (27)$$

where σ is a scale factor, $V(\theta_i)$ is the signal at angle θ_i, $V_b(\theta_i)$ is the background signal for that angle, and $I_e(\theta_i)$ is the experimental intensity at θ_i.

The scale factor was considered to be one of the parameters in the optimization procedure. The procedure was to minimize the function,

$$F(\alpha,m,\sigma) = \Sigma_i W_i |R_i|^2, \qquad (28)$$

where R_i is the residual defined by

$$R_i = I_e(\theta_i) - I_t(\theta_i), \qquad (29)$$

and W_i is a weighting function, which was taken to be $W_i = \sin^2\theta_i$.

To minimize the objective function, $F(\alpha,m,\sigma)$, the Marquardt-Levenberg routine performs an optimum interpolation between the Taylor series and gradient (steepest descent) methods. The computer code was run with various trial values in an attempt to find the global minimum of the function. To speed up the calculations the trial value of the optical size, α, was estimated from the measured aerodynamic size, which was obtained from the drag force experiments. A good trial value

---

[7]   Davis, E. J., and Ravindran, P., *Aerosol Sci. Tech.* **1**, 337 (1982).

[8]   Marquardt, D. W., *J. SIAM* **11**, 431 (1963).

of σ was obtained by rescaling the experimental maximum peak and minimum trough values to the maximum and minimum values for the angle range computed from Mie theory.   Usually, m_2, the imaginary component of the refractive index, was set equal to zero to start the computations.

Once the optimum values of α, m and σ were computed the phase function was calculated from Mie theory and compared with the experimental data to examine the quality of the "fit".   We shall present the results below.

An alternate, and simpler procedure, for determining a trial value of the light-scattering size was developed, which yielded accurate sizes for larger particles (a > 2 μm) and a reasonably good estimate of size for smaller particles. This technique was based on Mie theory computations for spheres of various sizes and refractive indices, which indicate that for large α the phase functions are relatively insensitive to refractive index but show a monotonically increasing number of peaks for a given angle range, say from 40° to 90°. Figure 11 presents the results of phase function computations for several refractive indices in the range of interest plotted as the number of peaks per 50° versus the optical size, α.   Thus, simply by counting the number of peaks over a 50° range it was possible to determine α within about 3% for α > 20.
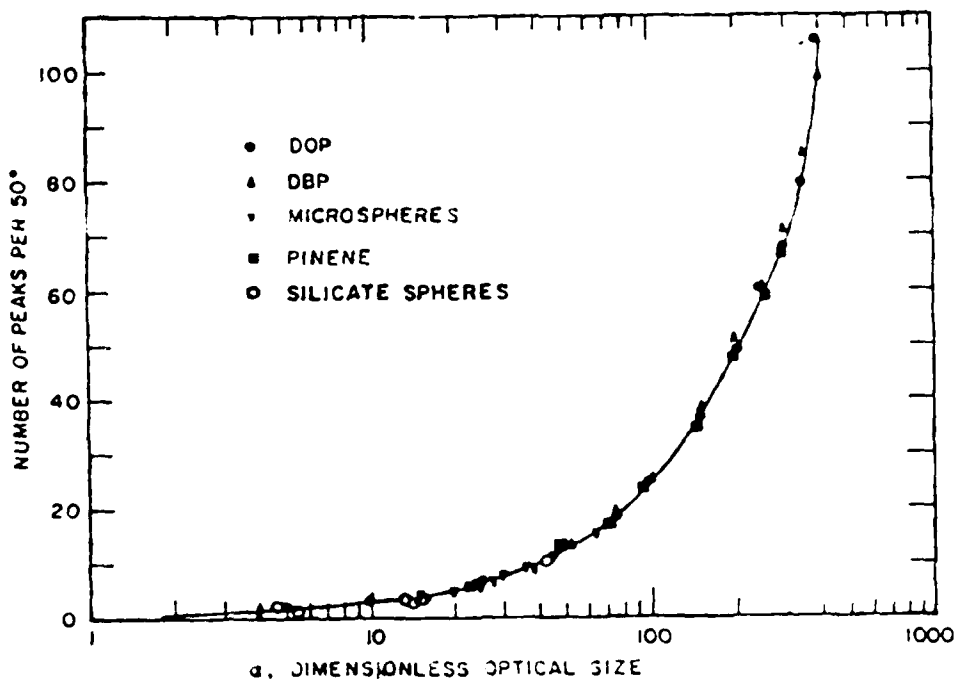

Figure 11. The number of phase function peaks per 50° as a function of α.

SECTION 3
RESULTS

3.1 SAMPLE IDENTIFICATION

The identification of the blow-off dust samples follows the notation used by SAI for data collection in the solar furnace experiments. Table 1 lists the run numbers, soil type and a description which indicates where the sample was taken from, for example, from an aerosol filter or from wall wipings. We shall identify each of our experiments by using the SAI run number together with an alphabetic character starting with A. For example, Sample 136C represents the third dust particle examined from SAI's run 136.

TABLE 1. Identification of samples.

SAI Run Number	Soil Type Code	Description
57	Silt P-14	Wall Wipings
60	Clay P-13	Wall Wipings
69	RB5I-2	Wall Collection
104	RC5Y-2	Wall Wipings
107	RC4U-2	Wall Wipings
136	Soil RBU2#15	Wall Wipings
138	Black Tile	Wall Wipings
1180	Wall-5F	Wall Wipings

3.2 PARTICLE CHARACTERIZATION

Each macroscopic sample of blow-off dust was examined in the scanning electron microscope to determine qualitatively the size distribution and shapes of particles. The microscope was equipped with energy dispersion x-ray spectrometry (EDAX) capabilities for elemental analysis. Figures 12a,b through 19a,b show repesentative results from the scanning electron microscope studies. We note that in most of the samples, with the possible exception of Runs 136 and 138, spherical particles are observed, indicating that the temperature in the solar furnace was high enough to melt many of these mixed silicates.

The EDAX analyses indicate that the samples were mostly mixed silicates of aluminum, calcium, magnesium and potassium. Iron was found in significant amounts in samples from Runs 60 and 136. Table 2 lists the results of EDAX analysis.

TABLE 2. Results of EDAX analysis.

Run Number	Elements Present in Sample
57	Al, Ca, K, Na, Si, Fe (trace)
60	Al, Ca, Fe, K. Si, Ag (trace)
69	Al, Ca, K, Na, Si, traces of Ag, Fe, Cu
104	Al, Si, Cu (trace)
107	Al, Ca. Si, traces of Cu, Fe
136	Al, Ca, Fe, K, Cu (trace)
138	Ag, Al, Ca, Si, Fe (trace)
1180	Al, Ca, Si, Cu (trace)

It is not possible to determine the types of minerals and their chemical formulas in the samples from the EDAX analyses because the EDAX results are qualitative, but it is reasonable to assume that minerals such as Andesine [$(CaO,Na_2O)Al_2O_3 \cdot 4SiO_2$], Anorthite ($CaO \cdot Al_2O_3 \cdot 2SiO_2$), Anorthoclase [$(Na,K)_2O \cdot Al_2O_3 \cdot 6SiO_2$)], Laboradorite ($NaAlSi_3O_8 + CaAl_2Si_2O_8$), Orthoclase ($K_2O \cdot Al_2O_3 \cdot 6SiO_2$), Kaolinite ($Al_2O_3 \cdot 2SiO_2 \cdot 2H_2O$), Gehlenite ($Ca_2Al_2SiO_7$) or other mixed silicates were present. The measured refractive indices are consistent with the bulk refractive indices of such minerals, as we shall show.
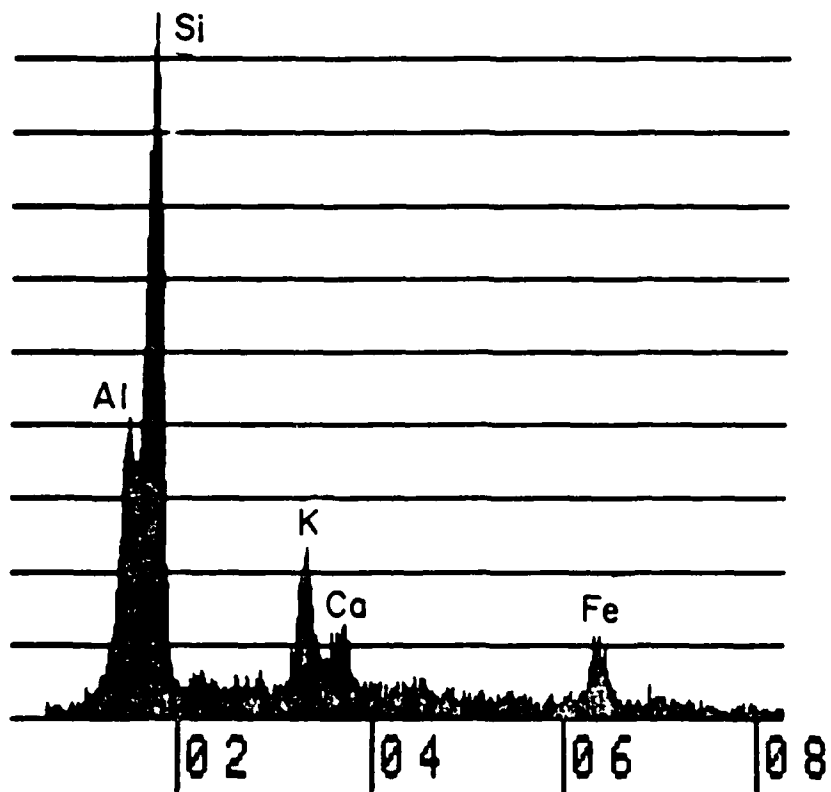
Figure 12 a,b.   A scanning electron micrograph (SEM) and EDAX analysis
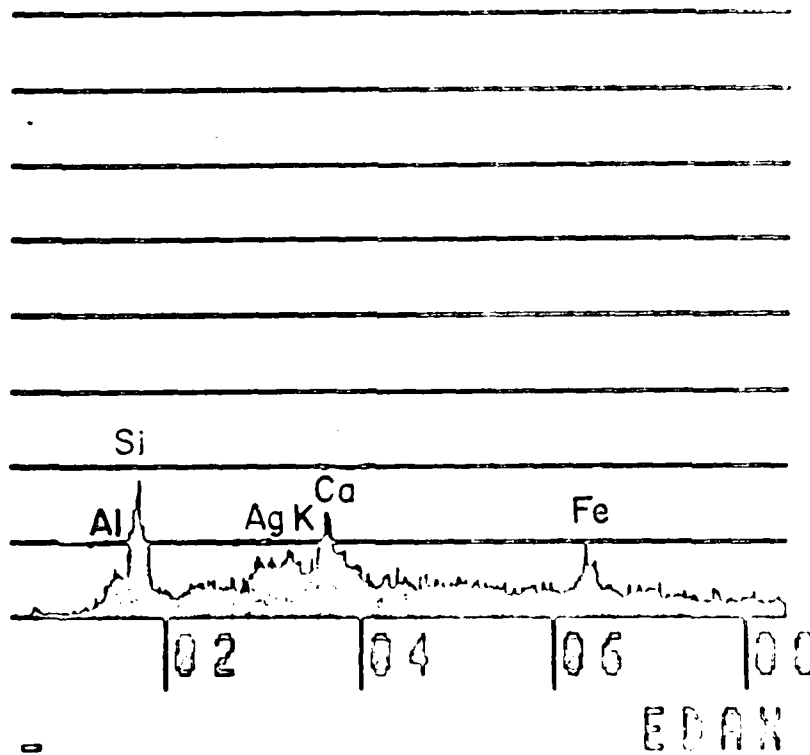for a wall wiping from Run 57.

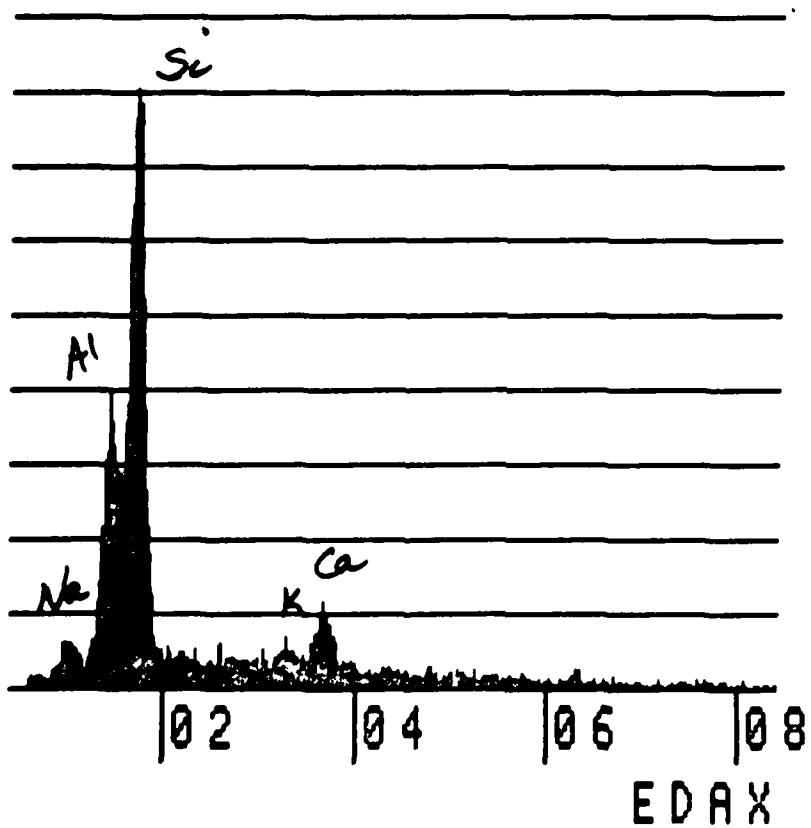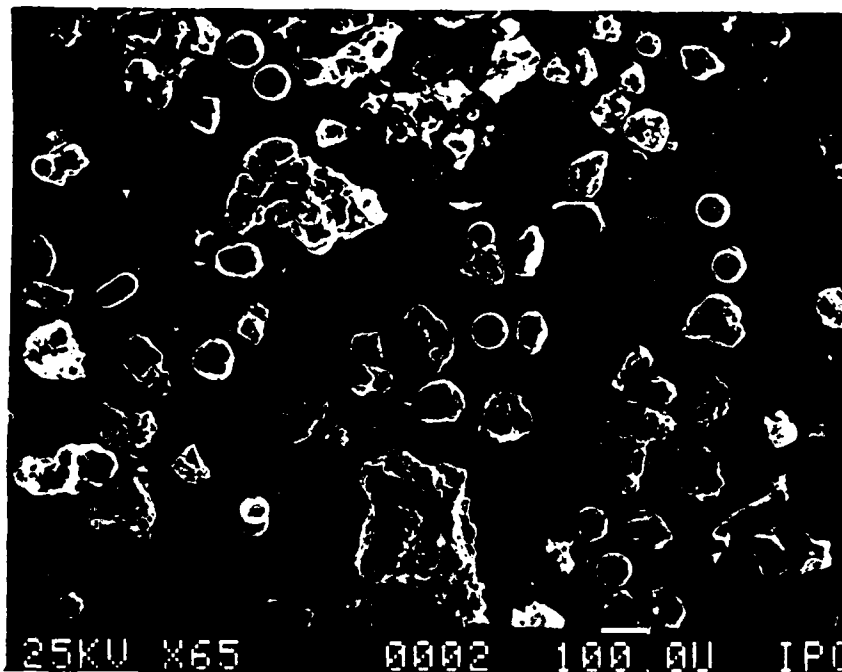Figure 13 a,b.   An SEM and EDAX analysis for a wall wiping from Run 60.

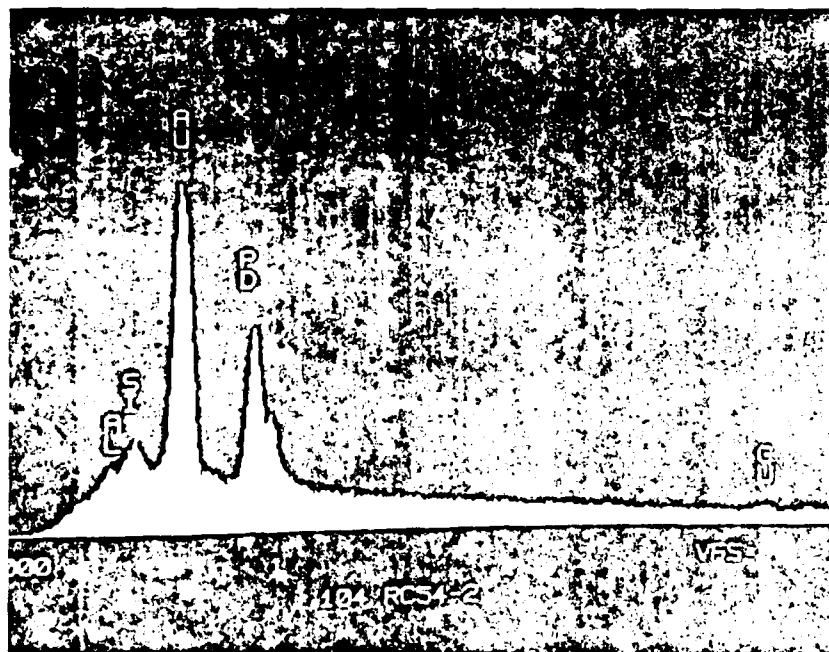Figure 14 a.b.   An SEM and EDAX analysis for a wall collection from Run 69

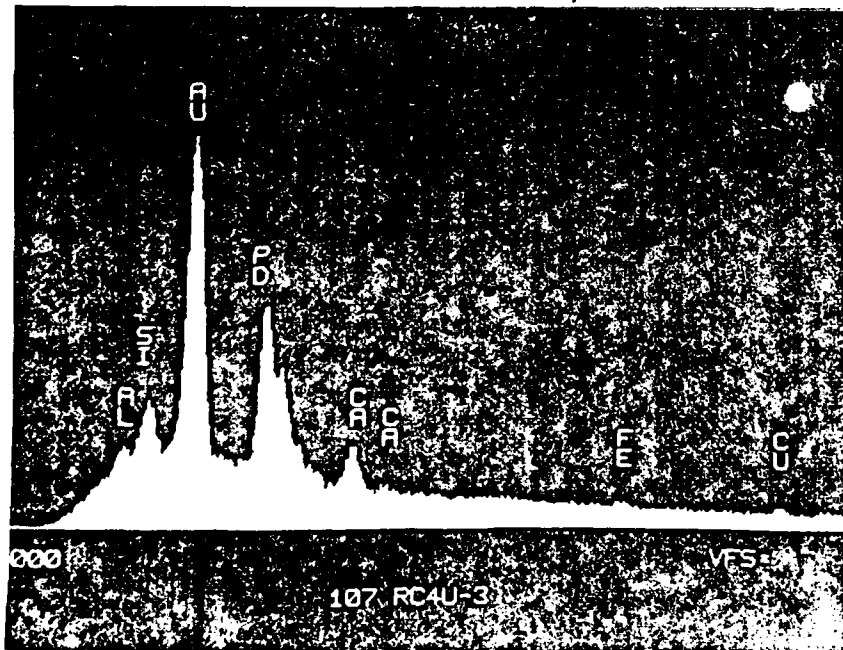Figure 15 a.b. An SEM and EDAX analysis for a wall wiping from Run 104.

23

Figure 16 a,b.   An SEM and EDAX analysis for a wall wiping from Run 107.
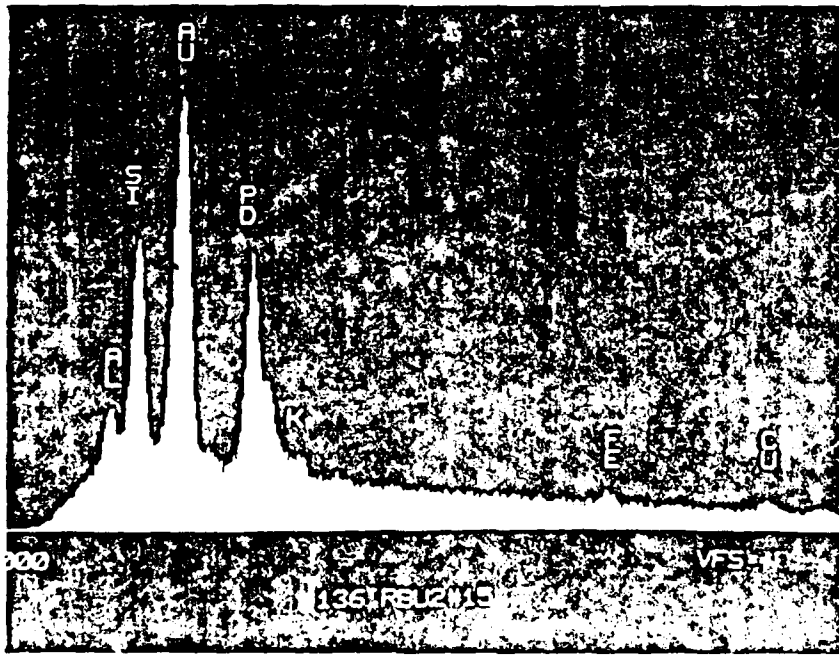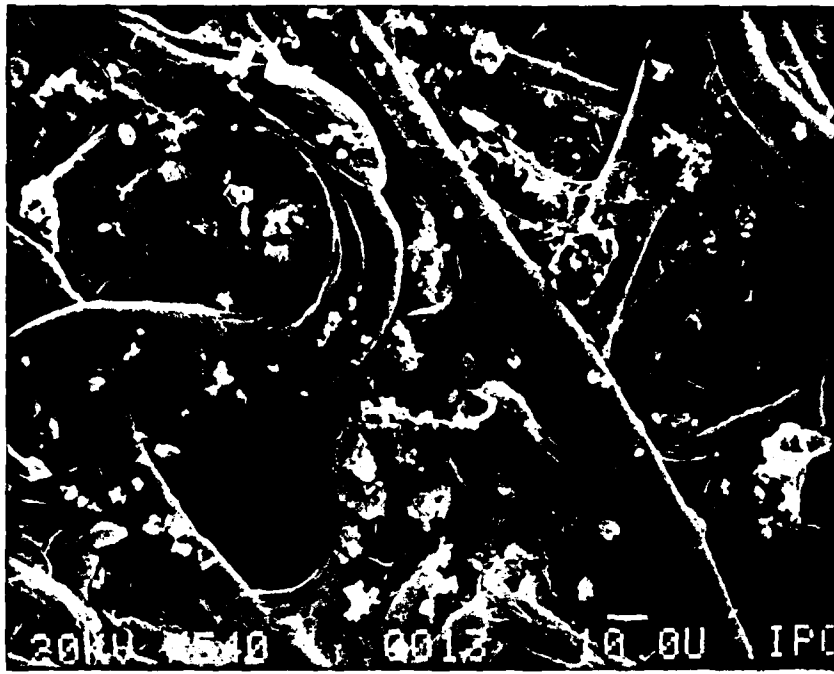
24

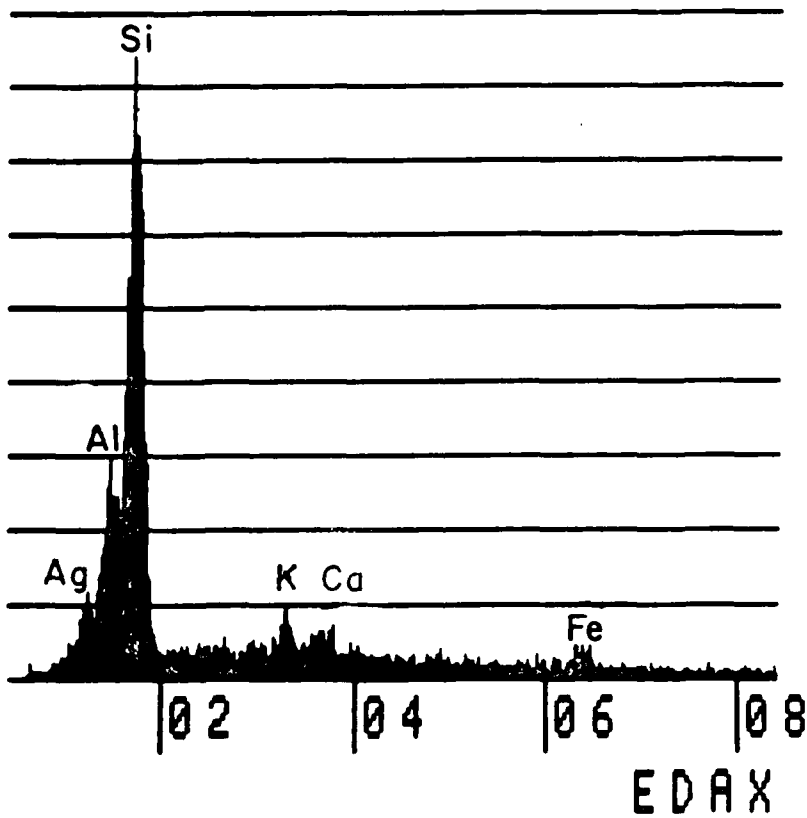Figure 17 a,b   An SEM and EDAX analysis for a wall wiping from Run 136.

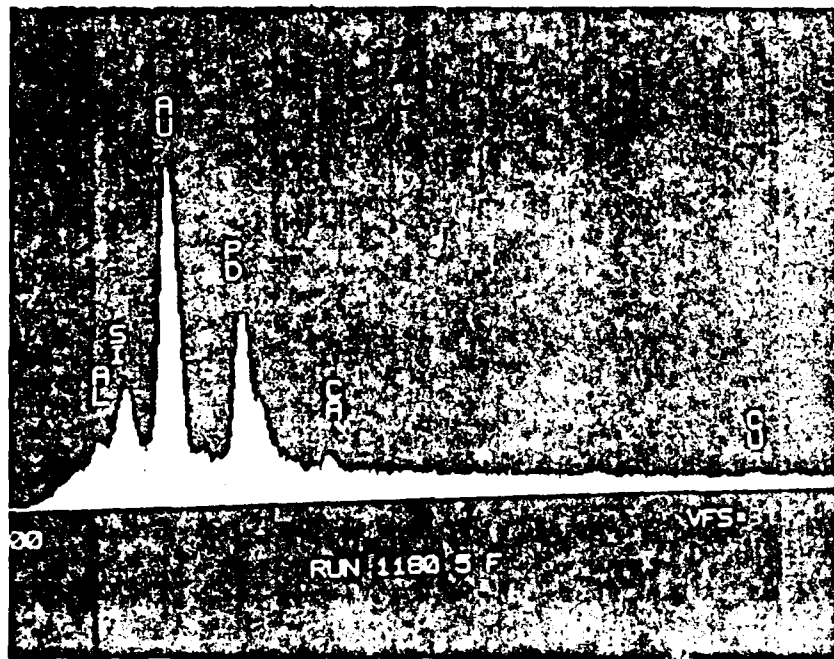Figure 18 a.b.   An SEM and EDAX analysis for a wall wiping from Run 138.

Figure 19 a.b.   An SEM and EDAX analysis for a wall wiping from Run 1180.

3.3 AERODYNAMIC DRAG CHARACTERISTICS

The ratio of the aerodynamic drag force, F_d, to the weight, mg, of a particle was obtained from the dc voltage data using Equation (19). The aerodynamic radius was calculated from the critical velocity, U_c required for the balance of the drag force and the gravitational force using Equation (20) or (21). Figures 20-27 show the ratio F_d/mg versus particle Reynolds number for numerous dust particles of various sizes and shapes from various soil samples. The particle Reynolds numbers were calculated using the measured aerodynamic radii. Because of the small sizes of the particles (a < 20 μm) the Reynolds numbers did not exceed 0.25, so all of the data were in the creeping flow regime. Figures 20-27 show that the drag forces are linear with respect to the Reynolds numbers. Additional results are provided in the Appendix.

To examine the effects of particle shape and roughness on the aerodynamic drag it is convenient to report the drag force in terms of the particle mobility, B, defined by

$$B = U_\infty/F_d. \tag{30}$$

For a spherical particle in the Stokes regime of creeping flow the mobility is given by

$$B = 1/6\pi a\mu, \tag{31}$$

but for nonspherical particles B depends on the shape and roughness.

The drag force can be calculated from the ratio F_d/mg as a function of gas velocity provided that we can determine the particle mass. The slope of a plot of F_d/mg versus U is given by l/Bmg. Thus, the reciprocal of the mobility is obtained by multiplying the measured slope by the particle weight, mg. For Figures 20-27, which have as the abscissae the Reynolds number rather than the velocity U, the slopes of the lines are inversely proportional to the particle mobility.

To calculate the mobility from the data on F_d/mg versus U the particle mass was estimated by assuming the particle to have the volume of a sphere having the same aerodynamic radius and a density equal to 2.855 g/cm^3, the average density of silicates with the elemental composition and refractive indices of the particles examined in this study. Table 3 summarizes the mobilities calculated in this way compared with the Stokesian mobilities obtained using the aerodynamic radii substituted in Equation (31). For spherical particles the two mobilities should be identical if the assumed density is correct.

28

For most of the data listed in Table 3 the mobilities based on Stokesian drag do not differ greatly from the mobilities computed from the drag force data, but there are a few exceptions. Particles 57A, 57F, 60J, 1180B and 1180F had mobilities at least 30% lower than those calculated from Stokes' law, and several other particles had mobilities at least 20% lower. Some of these discrepancies are due to uncertainties in the particle size and density.

Many of the particles listed as irregularly shaped in Table 3 had mobilities close to those predicted using Stokes' law, for example, irregular particles 60G, 60K, 60T, 60U, 69C, 69E, 69G, 69I, 104B, 107E, 136B, 136C, 136F, 138E, 1180C, 1180D and 1180E. From this result it is concluded that most of the particles were sufficiently similar to spheres to have the drag characteristics of spheres.
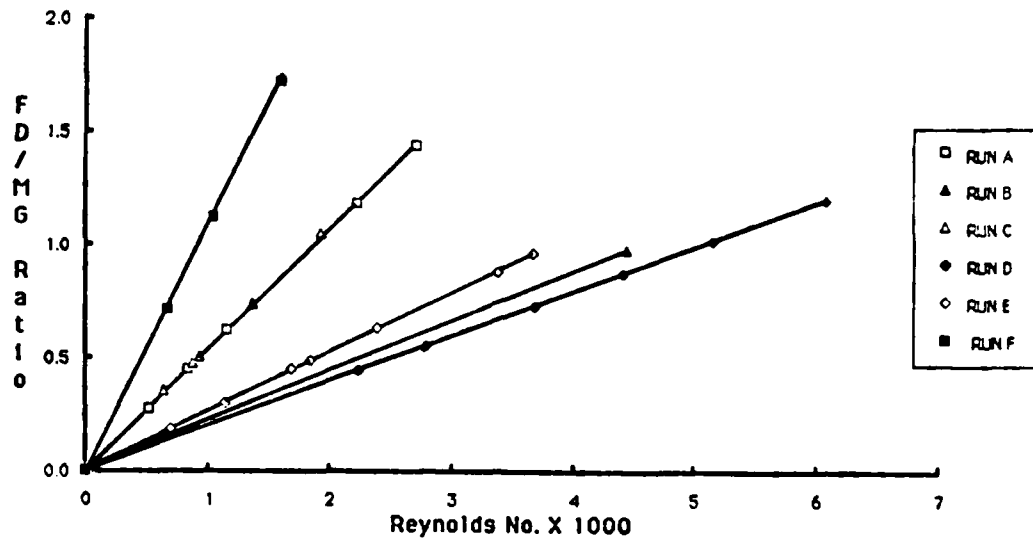
SAMPLE 57

Figure 20.   The ratio of the drag force to particle weight as a function of
the particle Reynolds number for particles from Sample 57.
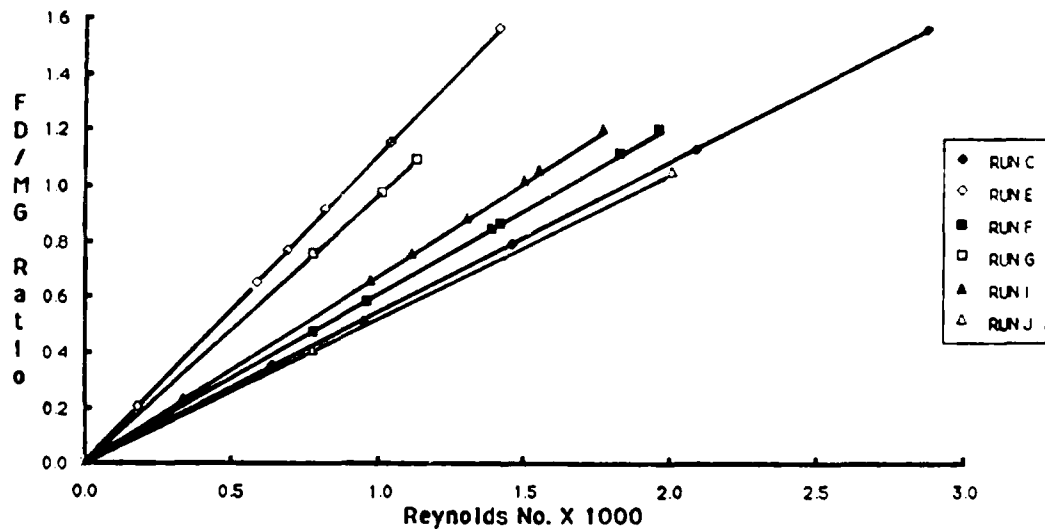
SAMPLE 60

Figure 21.   The ratio of the drag force to particle weight as a function of
the particle Reynolds number for particles from Sample 60.
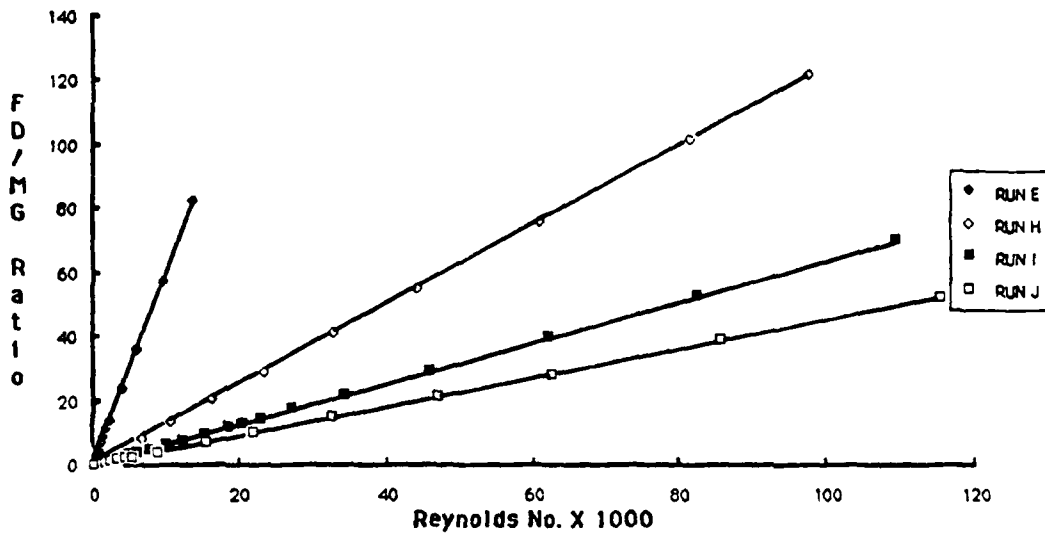
30

SAMPLE 69

Figure 22.   The ratio of the drag force to particle weight as a function of
the particle Reynolds number for particles from Sample 69.

SAMPLE 104

Figure 23.   The ratio of the drag force to particle weight as a function of
the particle Reynolds number for particles from Sample 104.
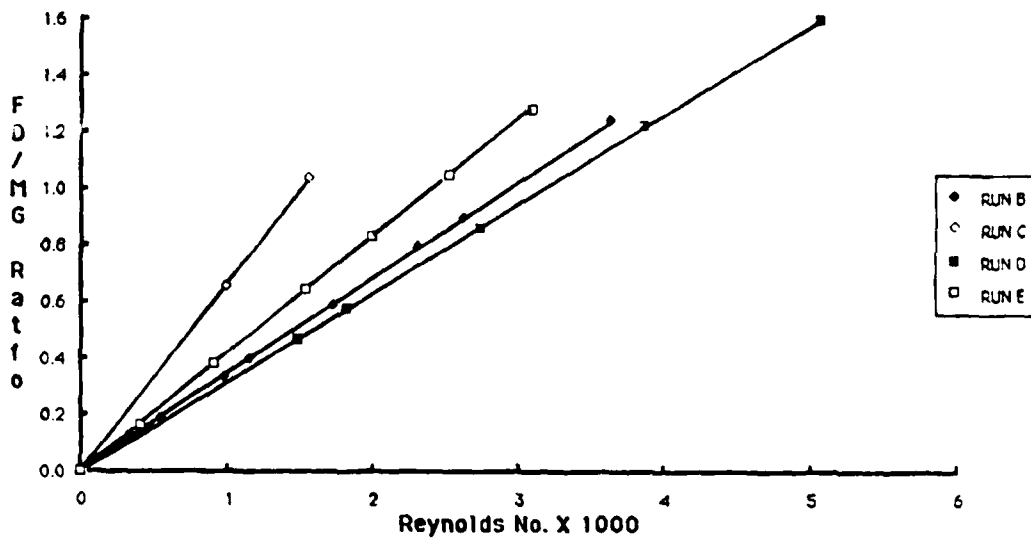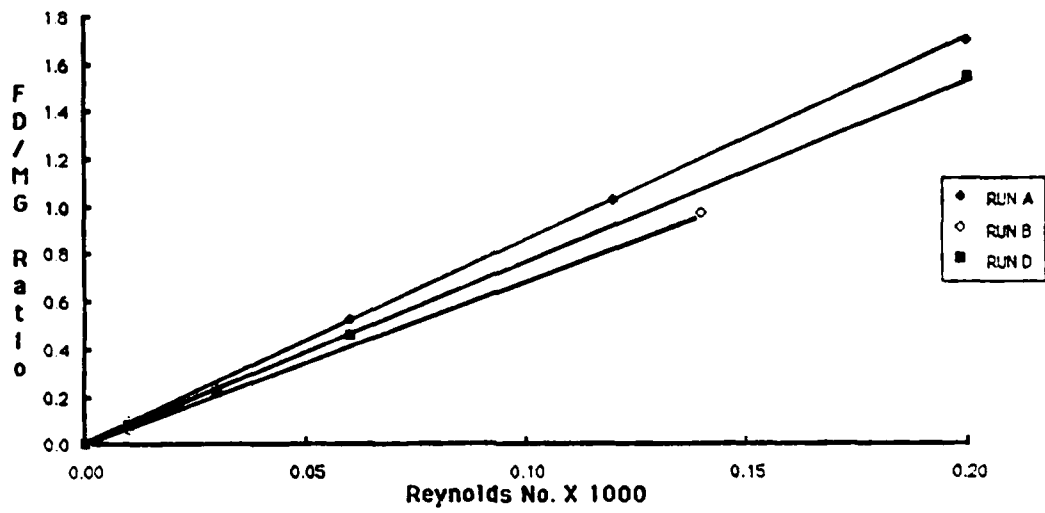
SAMPLE 107

Figure 24.   The ratio of the drag force to particle weight as a function of
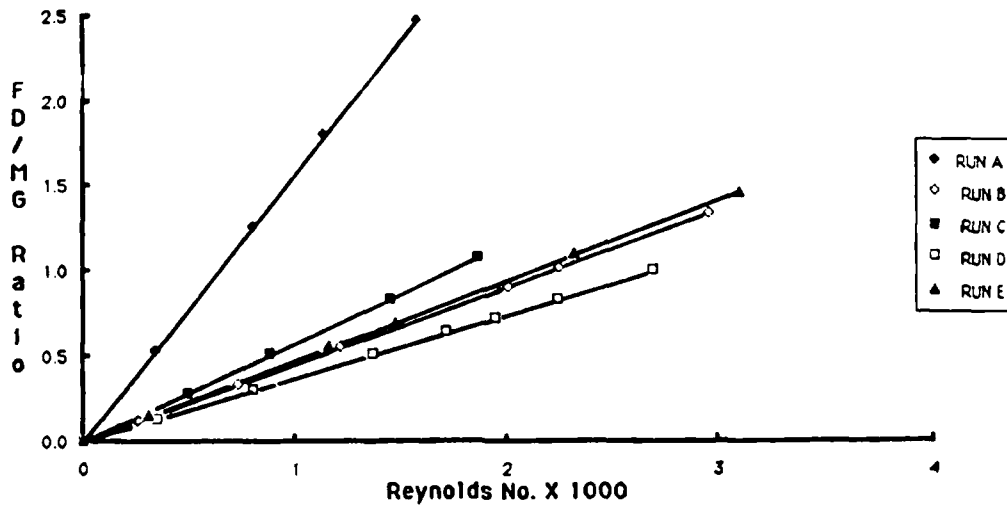the particle Reynolds number for particles from Sample 107.

SAMPLE 136

Figure 25.   The ratio of the drag force to particle weight as a function of
the particle Reynolds number for particles from Sample 136.
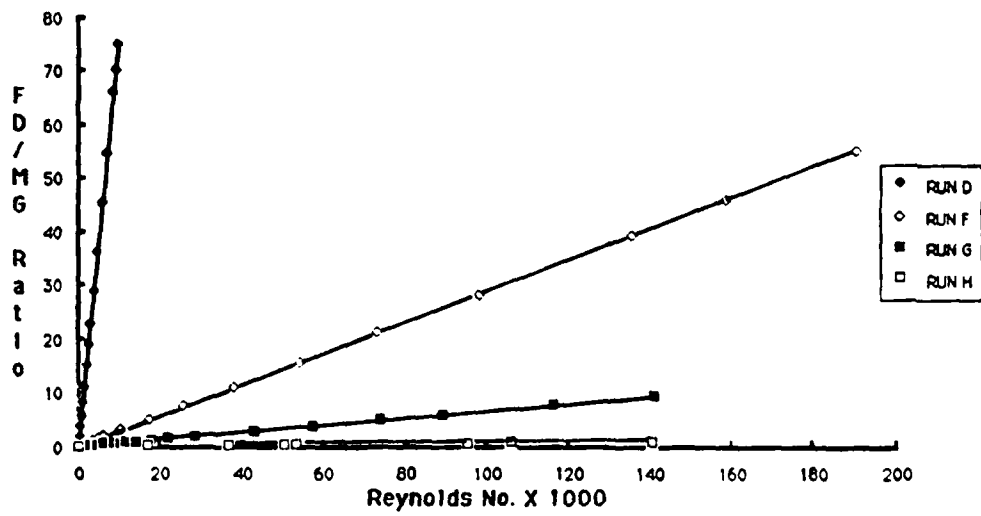
SAMPLE 138

Figure 26.   The ratio of the drag force to particle weight as a function of
the particle Reynolds number for particles from Sample 138.
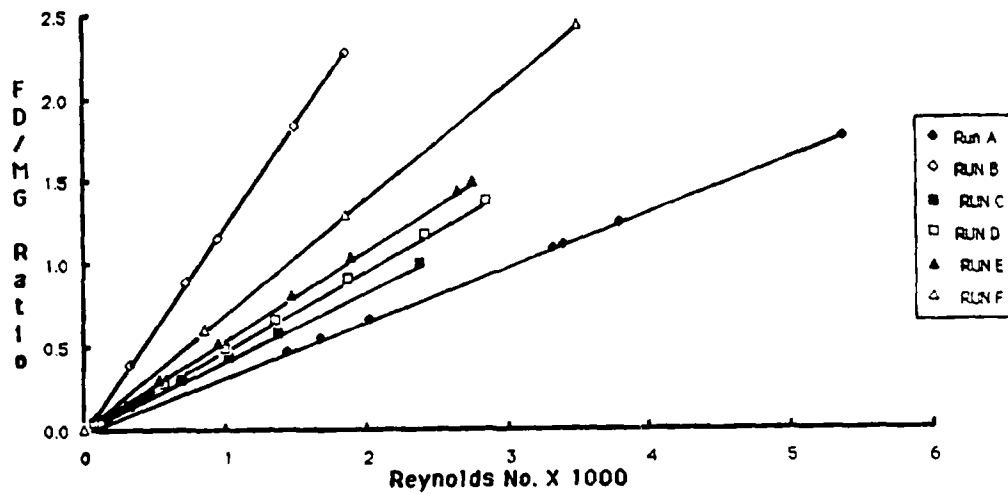
SAMPLE 1180

Figure 27.   The ratio of the drag force to particle weight as a function of
the particle Reynolds number for particles from Sample 1180.

33

TABLE 3. The radii and mobilities of dust particle.

Sample	Aerodynamic Radius, μm	Light Scattering Radius, μm	Stokes Mobility, Eq. (31) $s/g \times 10^{-6}$	Mobility, Eq. (30) $s/g \times 10^{-6}$	Shape
57A	3.78	3.32	0.915	0.634	Spherical
57B	4.46	-	0.303	0.274	Irregular
57C	3.31	3.52	0.920	0.904	Spherical(?)
57D	4.30	3.91	0.707	0.715	Spherical
57E	3.39	3.56	0.897	0.873	Spherical(?)
57F	2.67	2.44	1.14	0.689	Spherical
57G	10.04	9.87	0.303	0.274	Spherical
60A	-	4.24	0.718	-	Spherical
60B	1.56	1.79	1.95	1.960	Spherical
60C	3.51	3.76	0.867	0.610	Irregular
60D	1.67	2.21	1.82	1.83	Spherical
60E	3.33	2.60	0.914	0.891	Spherical
60F	3.18	-	0.957	0.886	Irregular
60G	2.72	-	1.116	1.12	Irregular
60H	4.18	-	0.726	0.690	Irregular
60I	4.30	3.07	0.707	0.786	Spherical(?)
60J	4.10	2.59	0.74 .	0.473	Irregular
60K	1.66	-	1.83	1.71	Irregular
60L	1.12	2.17	2.72	2.54	Spherical
60M	1.79	-	1.70	-	Irregular
60N	1.99	-	1.53	-	Irregular
60P	2.42	-	1.26	-	Irregular
60Q	12.6	-	2.43	-	Fiber(?)
60R	0.394	-	7.72	8.50	Irregular
60S	1.13	-	2.70	-	Irregular
60T	4.67	-	0.651	0.650	Irregular
60U	0.792	-	3.84	3.61	Irregular
69A	5.42	-	0.560	0.668	Irregular
69B	18.3	-	0 166	0.126	Aggregate(?)
69C	3.17	5.27	0.577	0.533	Spherical(?)

TABLE 3. The radii and mobilities of dust particle (Continued).

Sample	Aerodynamic Radius, μm	Light Scattering Radius, μm	Stokes Mobility, Eq. (31) s/g x 10^{-6}	Mobility, Eq. (30) s/g x 10^{-6}	Shape
69D	4.35	-	0.699	0.783	Rodlike(?)
69E	1.49	1.48	2.05	2.05	Spherical
69F	6.03	6.24	0.504	0.499	Spherical
69G	4.60	-	0.660	0.717	Irregular
69H	2.51	2.60	1.21	1.23	Spherical
69I	3.12	-	0.974	1.09	Irregular
69J	3.50	3.42	0.868	0.867	Spherical
69K	0.582	-	0.522	-	Irregular
104A	1.43	1.55	2.13	2.19	Spherical
104B	3.85	-	0.789	0.810	Irregular
104C	3.09	2.60	0.984	0.835	Spherical(?)
104D	3.96	3.76	0.768	0.757	Spherical(?)
104E	3.85	3.62	0.789	0.786	Spherical
107A	3.61	1.33	0.842	0.608	Spherical
107B	6.86	1.40	0.443	0.449	Spherical
107C	5.80	6.00	0.507	0.520	Spherical
107D	5.23	1.36	0.582	0.417	Spherical
107E	5.23	-	0.582	0.551	Irregular
136A	2.74	2.32	1.11	1.13	Spherical
136B	3.52	-	0.864	0.778	Irregular
136C	3.15	-	0.936	0.852	Irregular
136D	3.85	2.84	0.789	0.847	Spherical
136E	3.31	3.47	0.920	0.781	Spherical
136F	4.96	-	0.612	0.612	Irregular
136G	4.61	6.24	0.660	0.608	Spherical
136H	1.73	-	1.76	1.35	Irregular
138A	6.10	5.78	0.495	0.584	Spherical
138B	3.26	3.90	0.932	0.775	Spherical
138C	1.47	1.32	2.07	2.08	Spherical

TABLE 3. The radii and mobilities of dust particle   (Concluded).

Sample	Aerodynamic Radius, μm	Light Scattering Radius, μm	Stokes Mobility, Eq. (31) $s/g \times 10^{-6}$	Mobility, Eq. (30) $s/g \times 10^{-6}$	Shape
138D	1.36	2.52	2.24	2.95	Spherical(?)
138E	0.428	-	7.10	7.05	Irregular
138F	4.08	4.23	0.745	0.744	Spherical
138G	6.63	-	0.458	0.333	Irregular
138H	14.0	-	0.217	0.288	Rod(?)
138I	1.88	1.86	1.62	1.62	Spherical
1180A	4.18	3.91	0.727	0.713	Spherical
1180B	3.02	2.52	1.01	0.654	Spherical
1180C	3.59	-	0.844	0.885	Irregular
1180D	3.43	-	0.886	0.885	Irregular
1180E	3.31	-	0.919	0.918	Irregular
1180F	3.04	-	0.999	0.410	Irregular

3.4 LIGHT SCATTERING RESULTS

The main light scattering results were reported under Phase II of the research program, but additional data were obtained at a wavelength of 605 nm in Phase III. The phase function data for all particles studied were analyzed using the optimization algorithm discussed in Section 2.2, and typical results are plotted in Figures 28-34. The experimental intensities are plotted for a discrete set of data points, and the "best fit" results from Mie theory are plotted as continuous curves on the figures. Additional comparisons are made in Appendix B.

The agreement between the experimental data and Mie theory is not as good as is usually obtained for liquid droplets, which are perfect spheres, for the dust particles are not likely to be perfectly spherical even if melted. Furthermore, the particles might be somewhat inhomogeneous due to partial crystallization, and that would affect the light scattering. In general, the positions of peaks and troughs match the computed phase functions, but the amplitudes do not match particularly well. Table 4 summarizes the findings for those particles for which the optimization program converged.
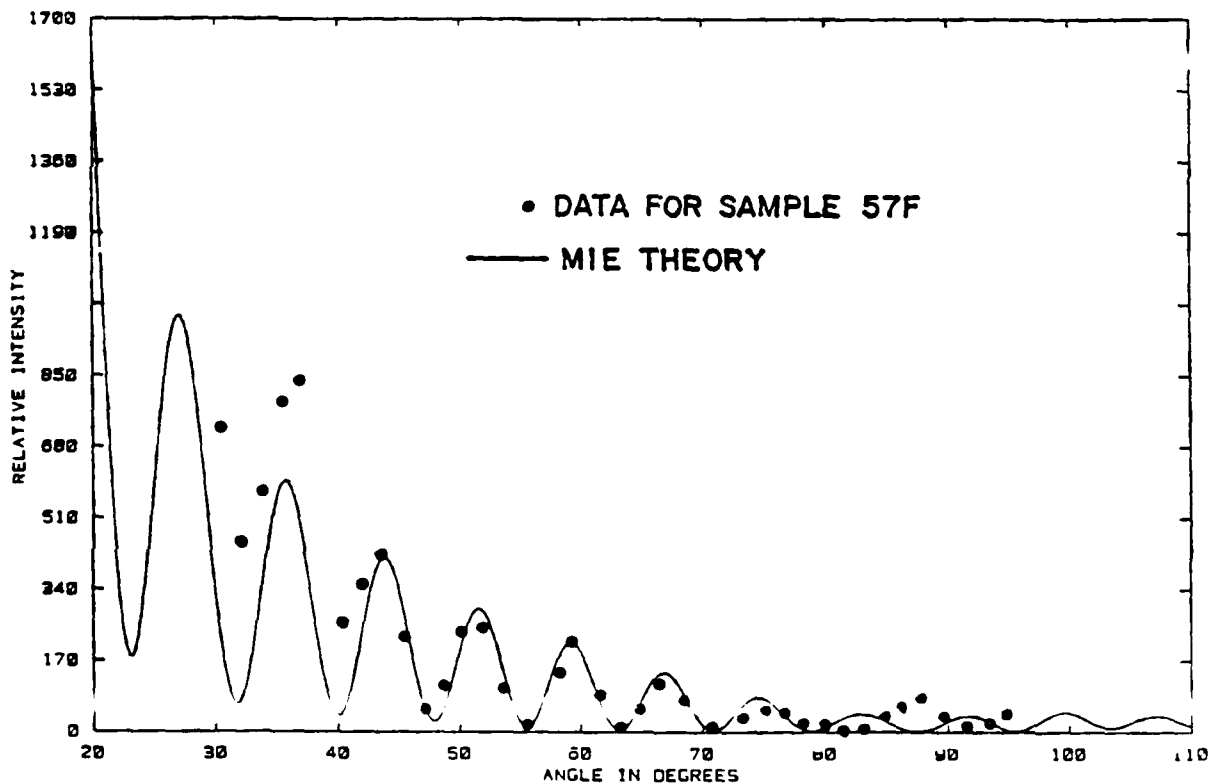
Figure 28. A comparison between light-scattering data for Sample 57F
and Mie theory for $\alpha = 25.3$ and $m = 1.4242 - i0.0057$.
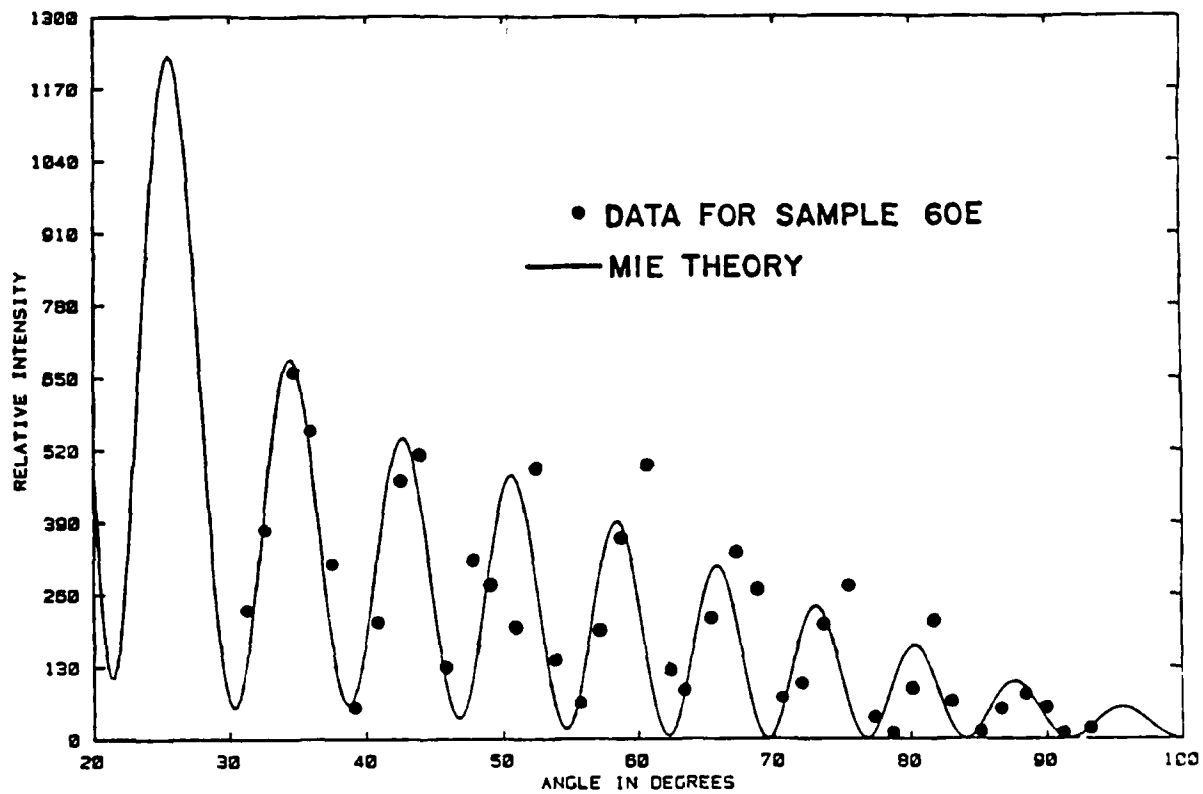
Figure 29. A comparison between light-scattering data for Sample 60E

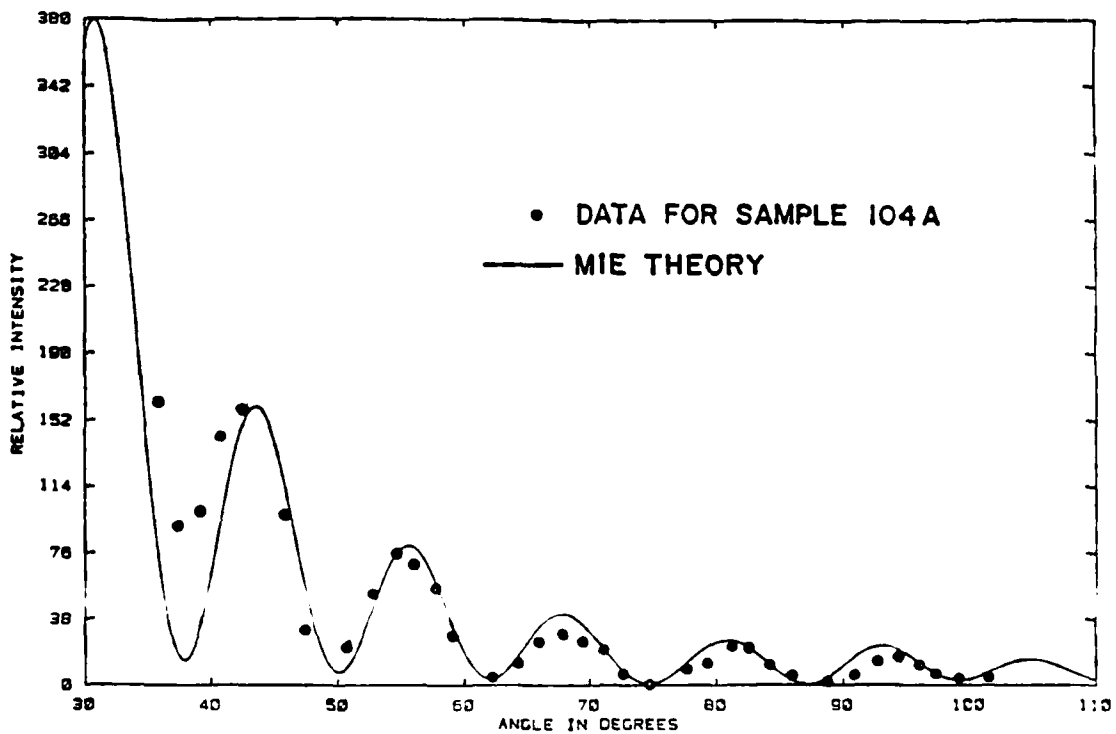and Mie theory for $\alpha = 27.0$ and $m = 1.6469 - i0.0038$.

Figure 30. A comparison between light-scattering data for Sample 104A

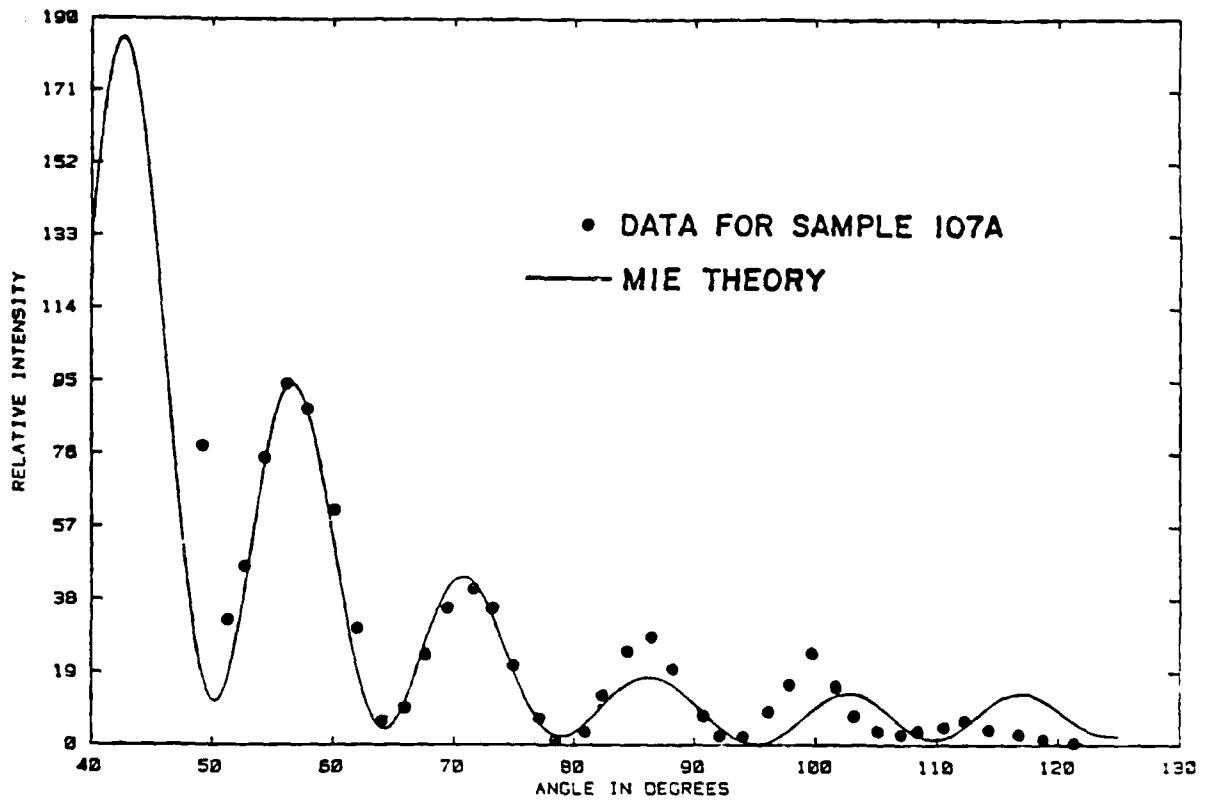and Mie theory for $\alpha = 16.1$ and $m = 1.3908 - i0.0091$.

Figure 31.   A comparison between light-scattering data for Sample 107A

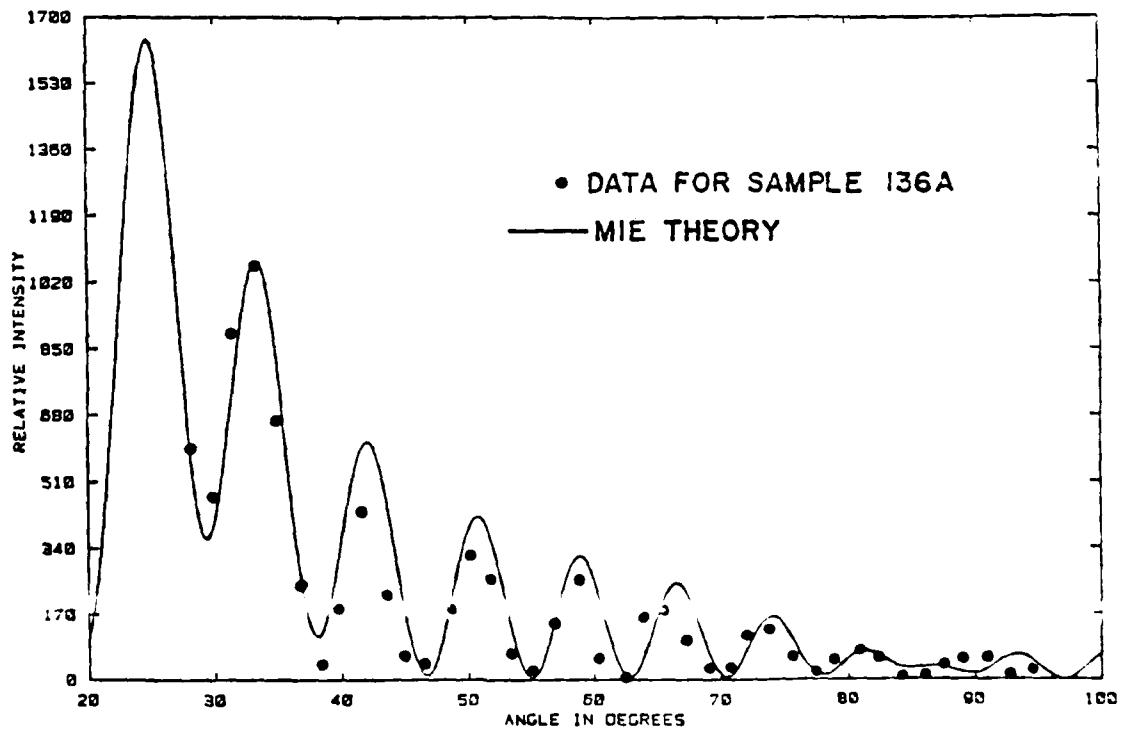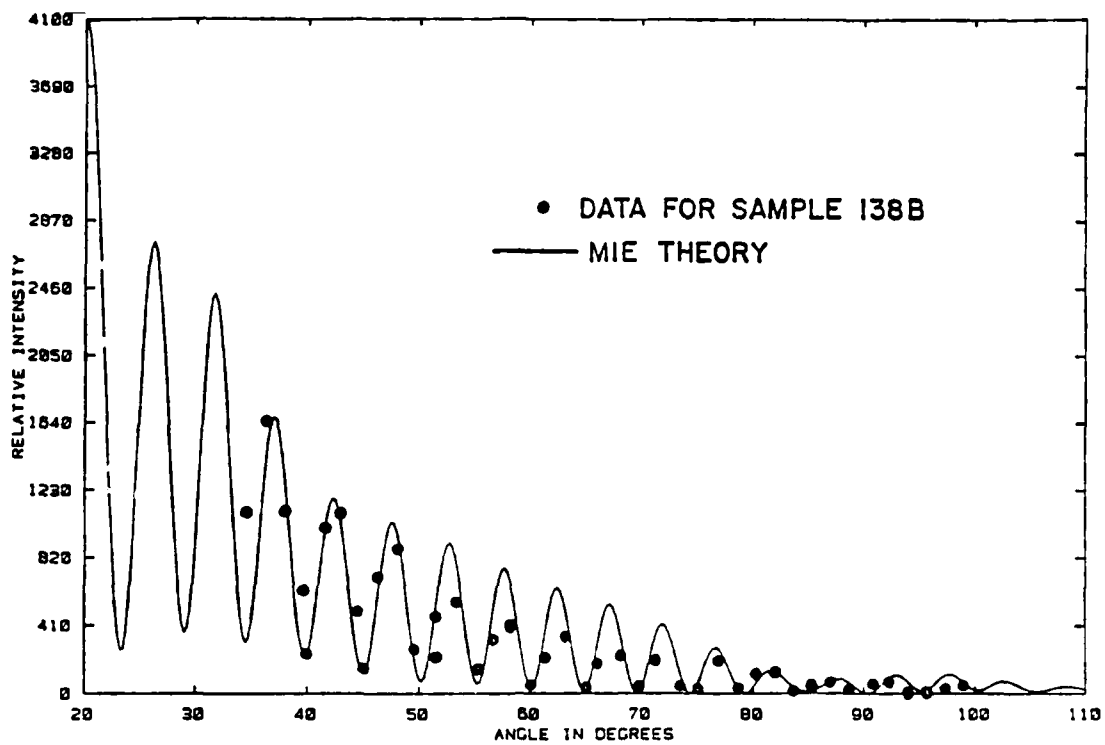and Mie theory for $\alpha = 13.8$ and $m = 1.6044 - i0.0093$.

Figure 32.   A comparison between light-scattering data for Sample 136A

and Mie theory for $\alpha = 24.1$ and $m = 1.5154 - i0.0007$.

Figure 33.   A comparison between light-scattering data for Sample 138B

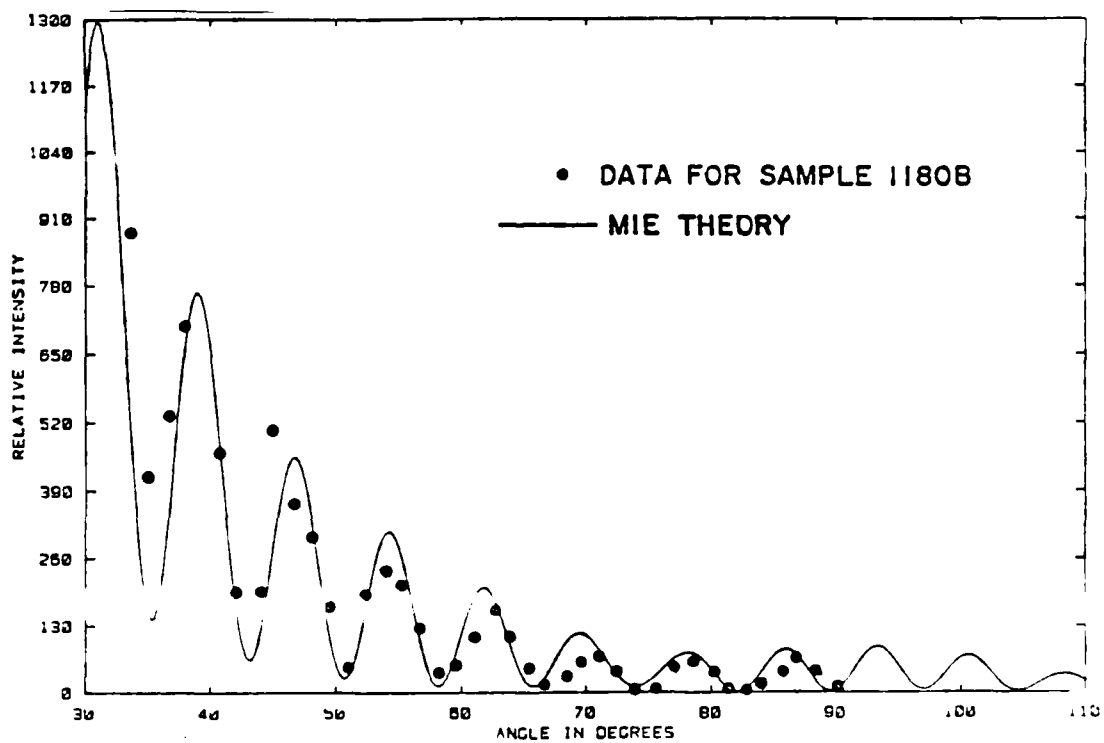and Mie theory for α = 40.5 and m = 1.5591 - i0.0022.

Figure 34.   A comparison between light-scattering data for Sample 1180B

and Mie theory for α = 26.2 and m = 1.4689 - i0.0030.

Table 4. Light scattering results for dust particles at a wavelength of
605 nm obtained by the optimization procedure.

Sample Number	α	Radius, μm	Refractive Index	Albedo
57A	34.5	3.32	1.4734 - i0.0081	0.675
57D	40.6	3.91	1.4574 - i0.0043	0.774
57F	25.3	2.44	1.4242 - i0.0057	0.786
60B	18.6	1.79	1.4157 - i0.0079	0.779
60D	22.9	2.21	1.4475 - i0.0009	0.956
60E	27.0	2.60	1.6469 - i0.0038	0.844
60I	31.8	3.07	1.5238 - i0.0018	0.896
60J	26.9	2.59	1.5725 - i0.0002	0.988
69E[a]	14.7	1.48	1.4832 - i0.0060	0.825
69H[a]	25.8	2.60	1.4238 - i0.010	0.700
104A	16.1	1.55	1.3908 - i0.0091	0.778
104E	37.6	3.62	1.6175 - i0.0015	0.899
107A	13.8	1.33	1.6044 - i0.0093	0.817
107B	14.5	1.40	1.6049 - i0.0042	0.897
107D	14.1	1.36	1.5457 - i0.0042	0.863
136A	24.1	2.32	1.5154 - i0.0007	0.964
136D	29.5	2.84	1.5047 - i0.0107	0.684
136E	36.1	3.47	1.5447 - i0.0018	0.886
138B	40.5	3.90	1.5591 - i0.0022	0.850
138C	13.7	1.32	1.3948 - i0.0169	0.737
1180A	40.6	3.91	1.5177 - i0.0045	0.771
1180B	26.2	2.52	1.4689 - i0.0030	0.880

---

a   Measured at a wavelength of 632.8 nm.

3.5 DISCUSSION OF RESULTS

The light-scattering data indicate that the real components of the refractive index, m_1, for a wavelength of 605 nm are in the range 1.3908-1.6469, which is consistent with the bulk values of the refractive index of various mixed silicates. For example, for the sodium line ($\lambda = 589.3$ nm) Andesine has a refractive index of 1.544-1.563, Anorthite 1.577-1.590, Anorthoclase 1.523-1.529, Orthoclase 1.518-1.539, Kaolinite 1.522-1.570, and Gehlenite 1.658-1.669. Data are not available with which to compare the imaginary component of the refractive index, but Mie theory computations indicate that the predicted phase function is not highly sensitive to the imaginary component for the low range of values estimated here. The main effect of the imaginary component, m_2, is to alter the scale factor or amplitude of the phase function and not the angular positions of peaks and troughs. Thus, the uncertainties in the reported values of m_2 are great, and the calculated albedos are not accurate. It should be concluded that the albedos are of order one, and there is essentially no significant energy absorption by the dust particles in the range of visible light.

The scanning electron micrographs show that for Samples 57, 60, 69, 104, 107 and 1180 many spherical particles were generated. Even those particles which had not melted to become spherical were more sphere-like than rod-like or disk-like, so their aerodynamic drag characteristics might be expected to approximate those of spheres. The experimental data and calculated mobilities indicate, indeed, that the particles behaved like spheres. Samples 136 and 138 (see Figures 17a and 18a) showed a wide variety of irregularly shaped particles, but the measured mobilities do not differ greatly from the Stokes mobility for spheres.

For the range of gas velocities which could be used with the electrodynamic balance, the Reynolds numbers were generally in the creeping flow regime, and the measured ratios F_d/mg were found to be linear functions of Reynolds number, which is characteristic of creeping flow. Very few particles were observed to have nonlinear drag characteristics (see Figure 10), and those which were not typical were probably extraneous particles such as small fibers from the filters or wall wiping material. It is to be expected that at higher Reynolds numbers all of the particles would have a nonlinear Reynolds number dependence.

For purposes of estimating the properties of blow-off dust particles it is recommended that the bulk refractive index be used for the types of minerals expected, that the single particle albedos be considered to be unity, and that the aerodynamic drag characteristics be taken as that of a sphere of the same volume as the dust particle in question.
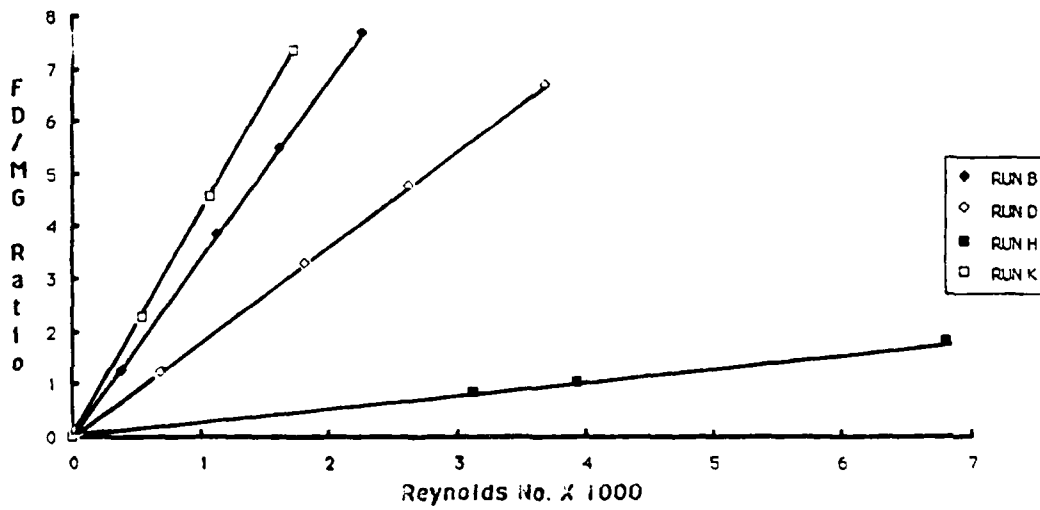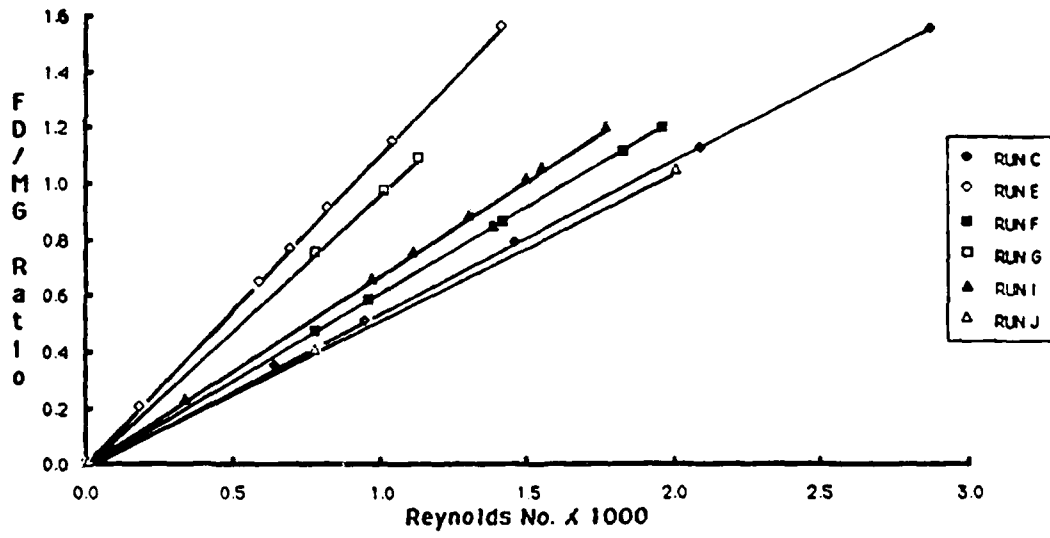
SUPPLEMENTARY DRAG DATA

SAMPLE 60
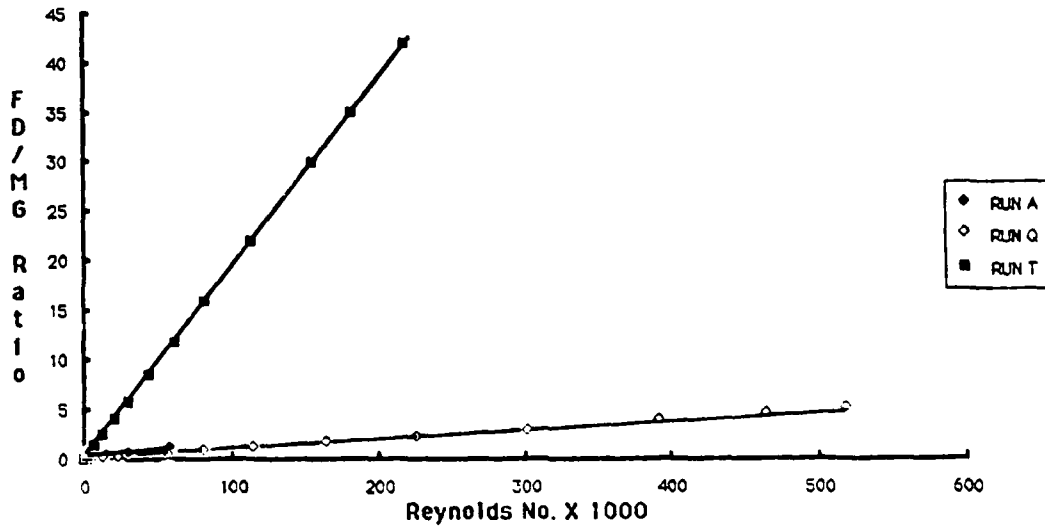
SAMPLE 60

Figure 35a,b.   Drag force data for Sample 60.
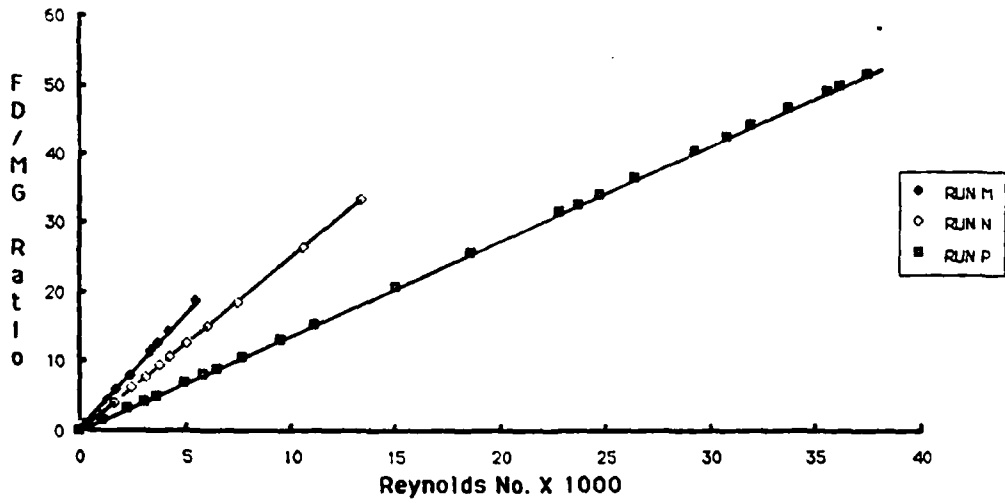
SAMPLE 60
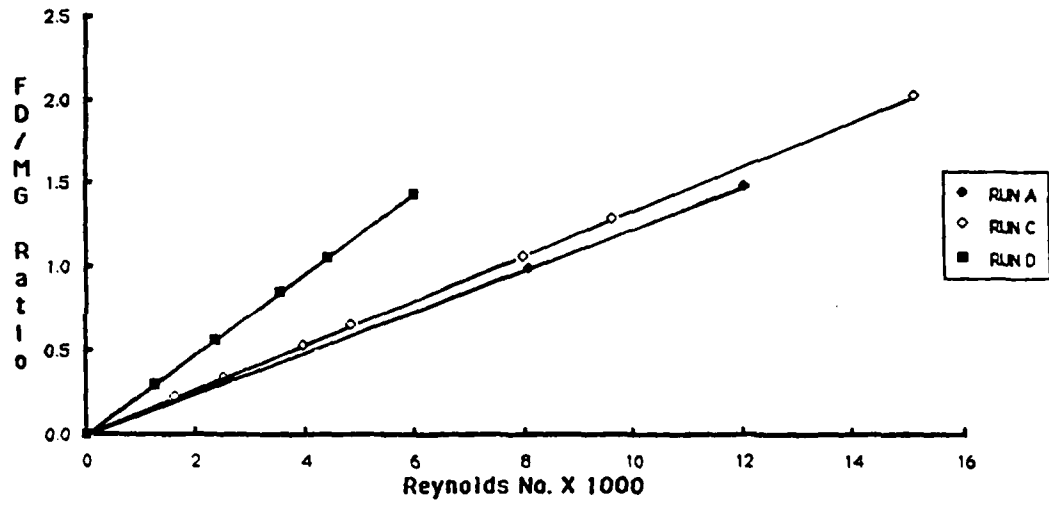

SAMPLE 60

Figure 36a,b.   Drag force data for Sample 60.
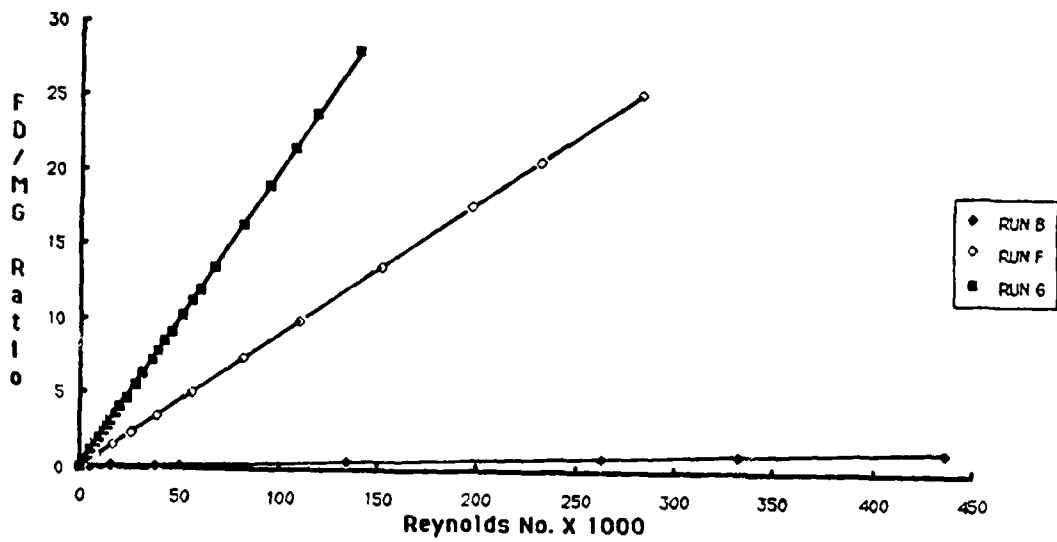
44

SAMPLE 69

SAMPLE 69

Figure 37a,b.   Drag force data for Sample 69.

45

SAMPLE 104, RUN A
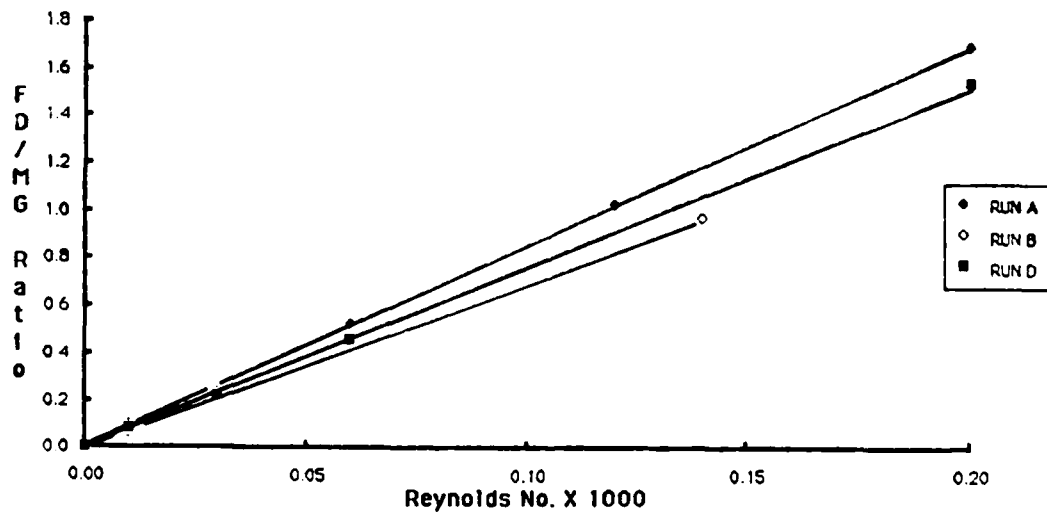
Figure 38. Drag force data for Sample 104.

SAMPLE 107
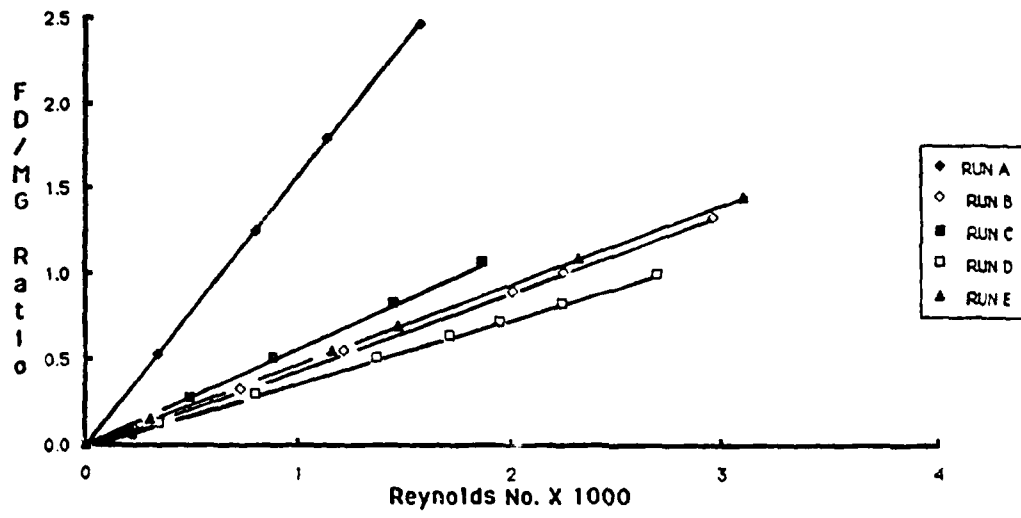
Figure 39. Drag force data for Sample 107.

46

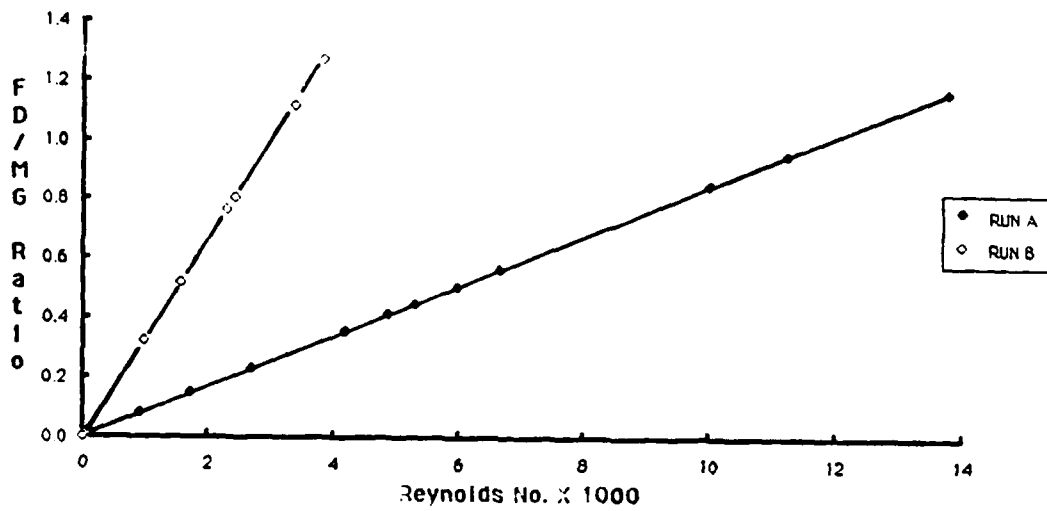## SAMPLE 136

Figure 40.   Drag force data for Sample 136.

SAMPLE 138

Figure 41.   Drag force data for Sample 138.
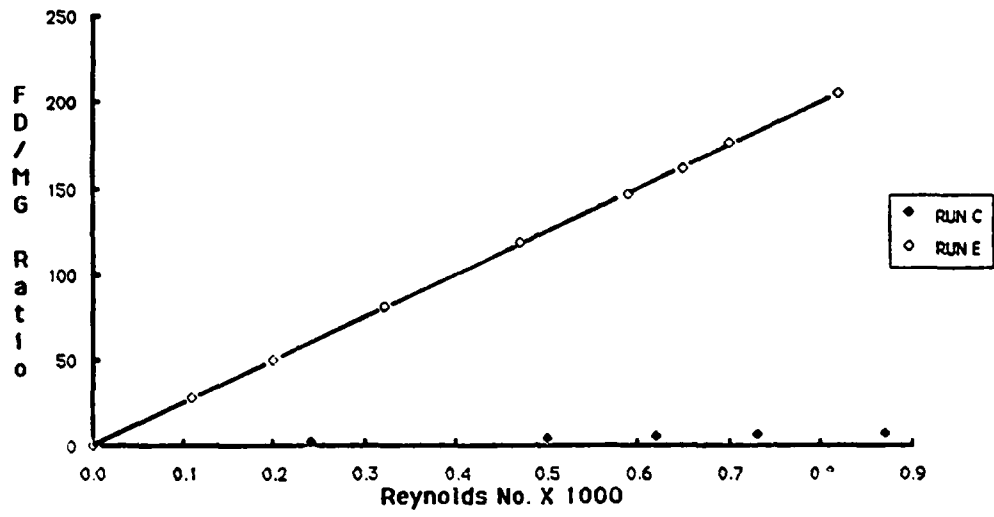
47

SAMPLE 138

Figure 42.   Drag force data for Sample 138.

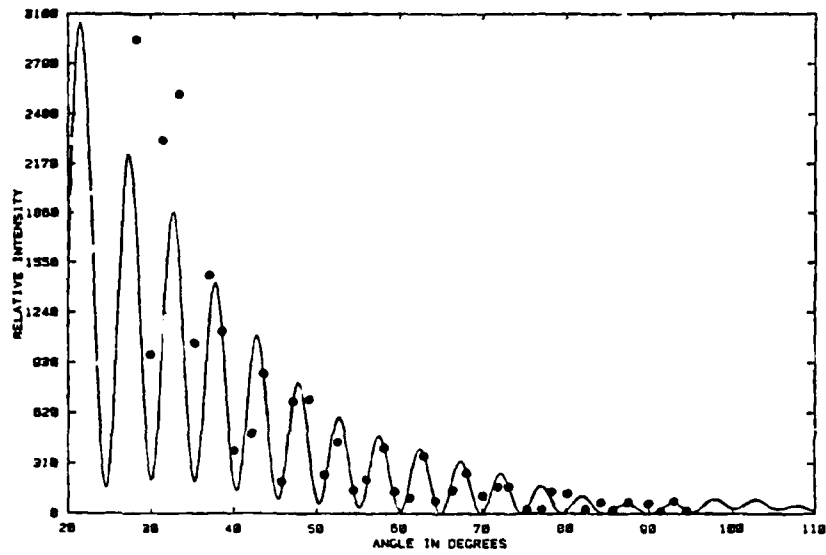SUPPLEMENTARY LIGHT-SCATTERING DATA

Figure 43.   Mie theory (————) for α = 40.6 and m = 1.4574 - i0.0043

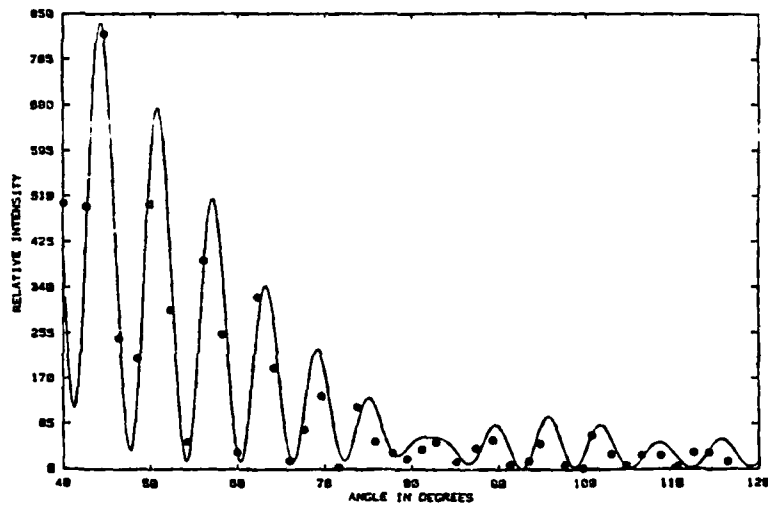compared with light-scattering data (•) for Sample 57D.

Figure 44.   Mie theory (————) for α = 31.8 and m = 1.5238 - i0.0018

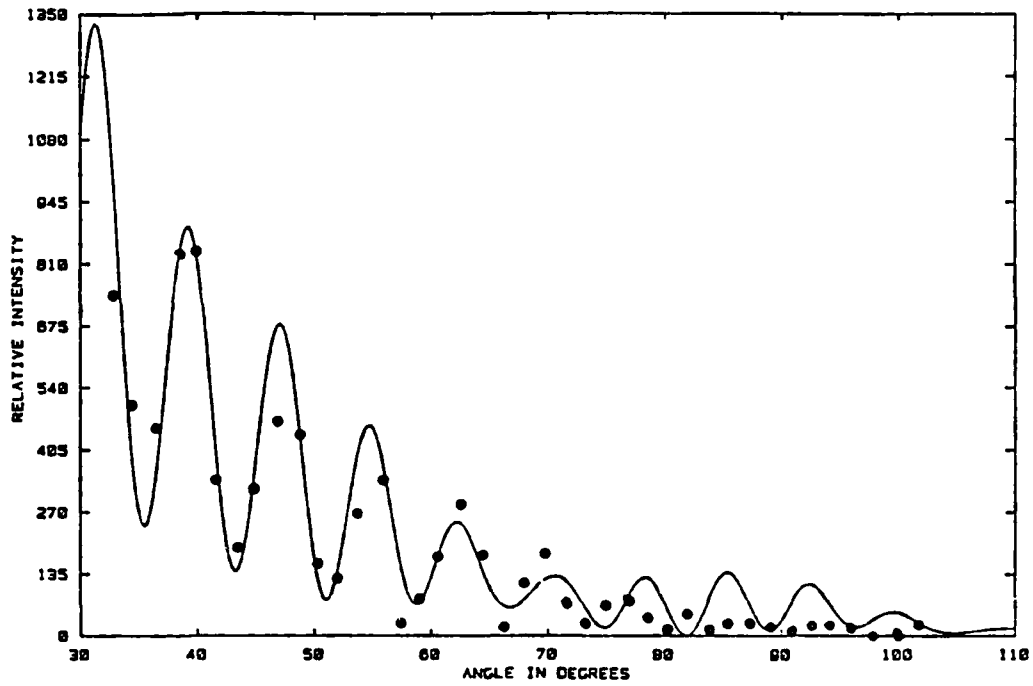compared with light-scattering data (•) for Sample 60I.

Figure 45. Mie theory (————) for α = 26.9 and m = 1.5725 - i0.0002
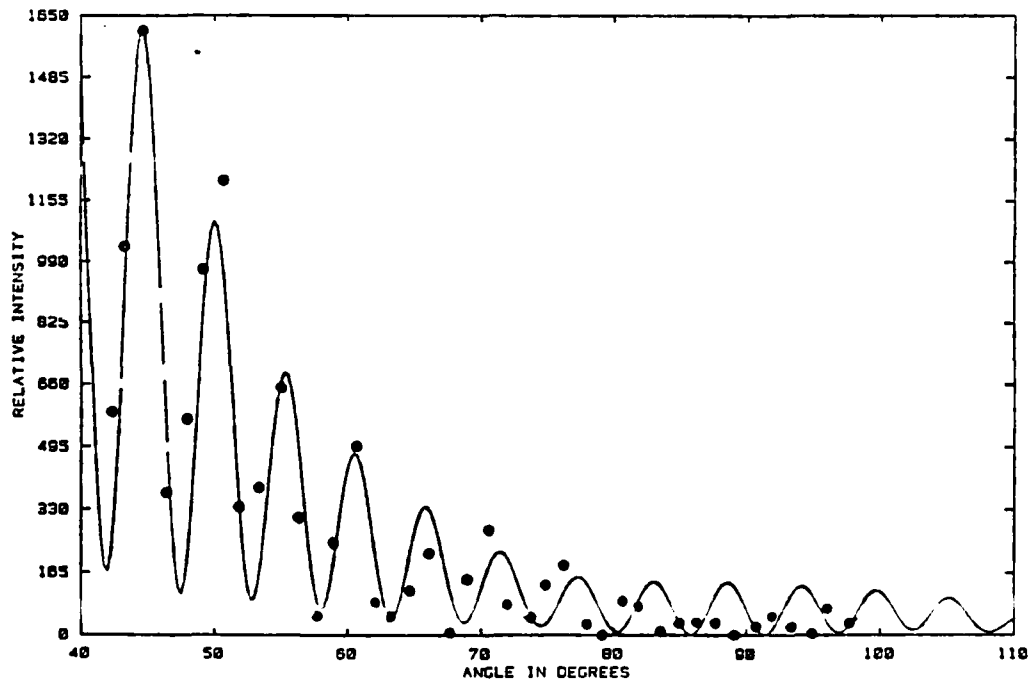compared with light-scattering data (•) for Sample 60J.

Figure 46. Mie theory (————) for α = 37.6 and m = 1.6175 - i0.00115
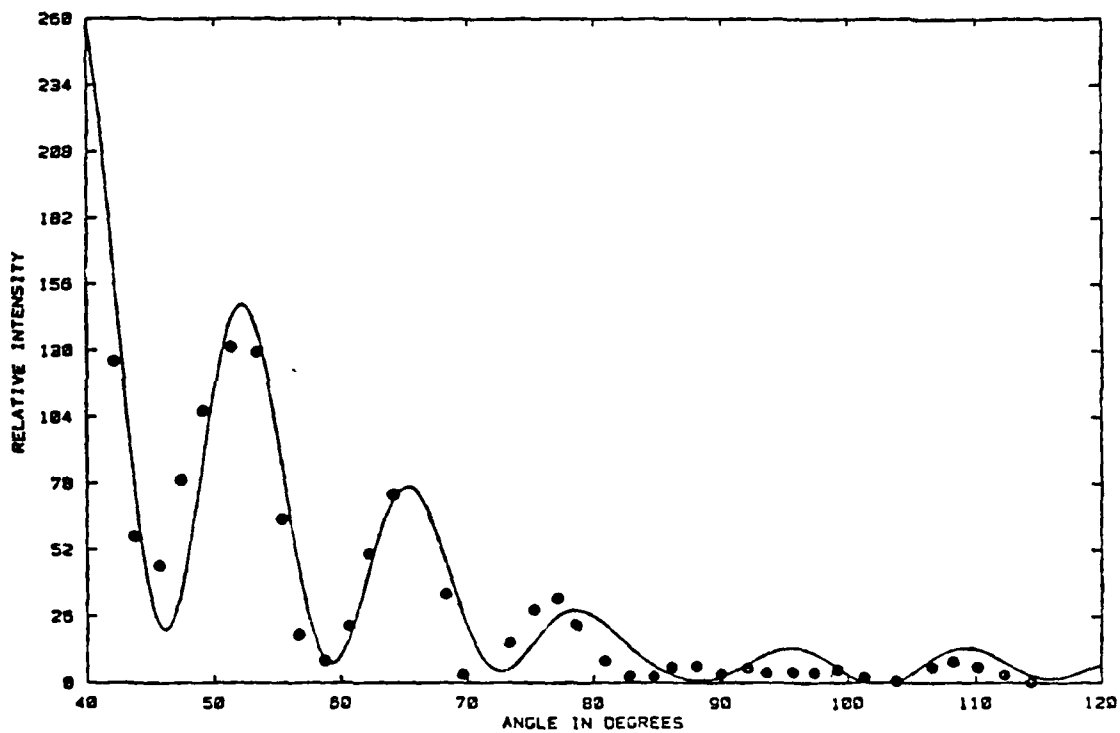compared with light-scattering data (•) for Sample 104E.

50

Figure 47.   Mie theory (————) for α = 14.5 and m = 1.6049 - i0.0042
compared with light-scattering data (•) for Sample 107B.
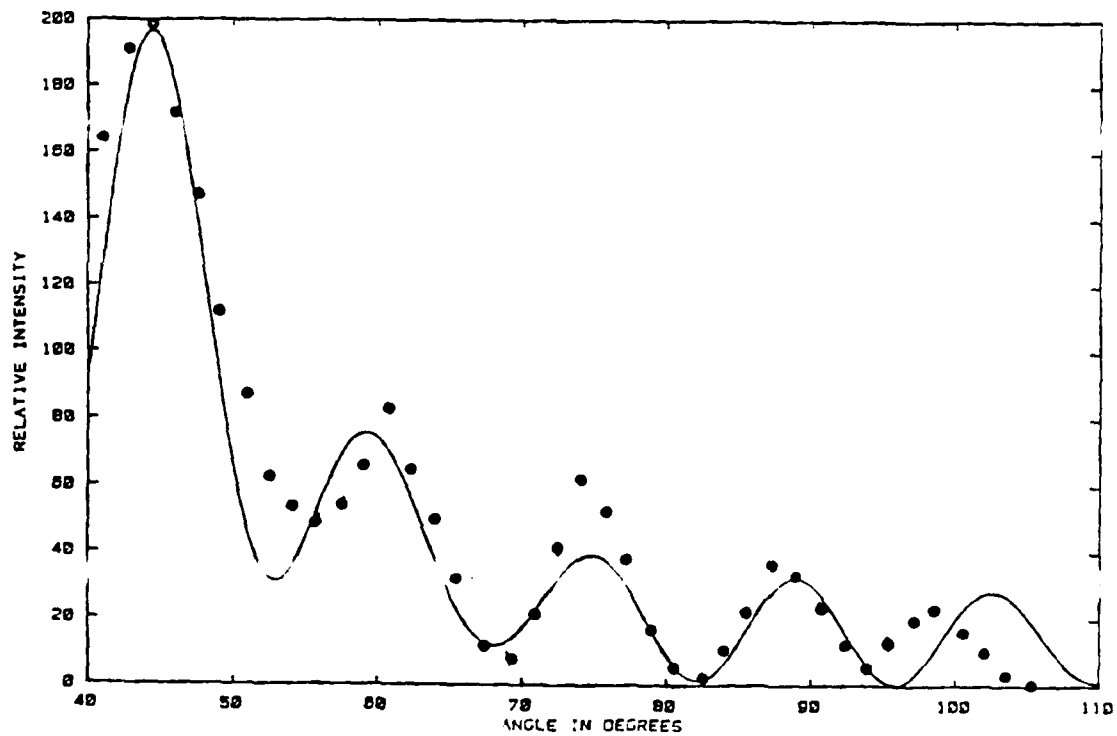

Figure 48.   Mie theory (————) for α = 14.1 and m = 1.5447 - i0.0042
compared with light-scattering data (•) for Sample 107D.

51

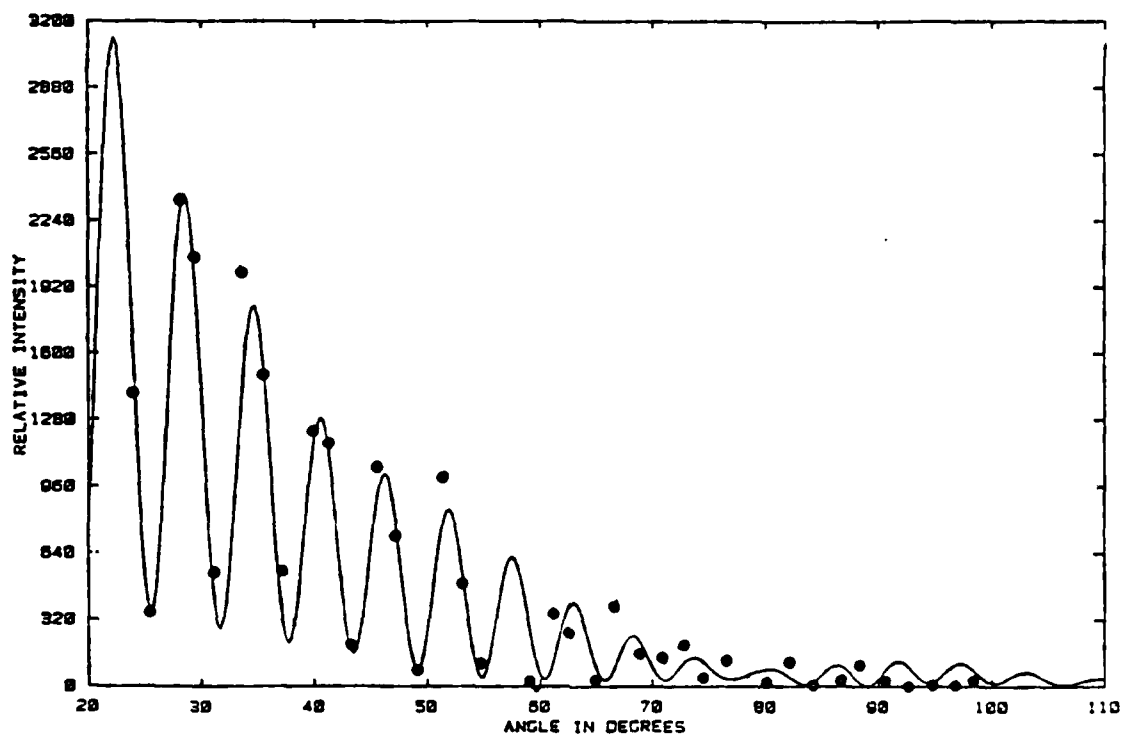Figure 49.   Mie theory (———) for α = 36.1 and m = 1.5447 - i0.0018

compared with light-scattering data (•) for Sample 136E.
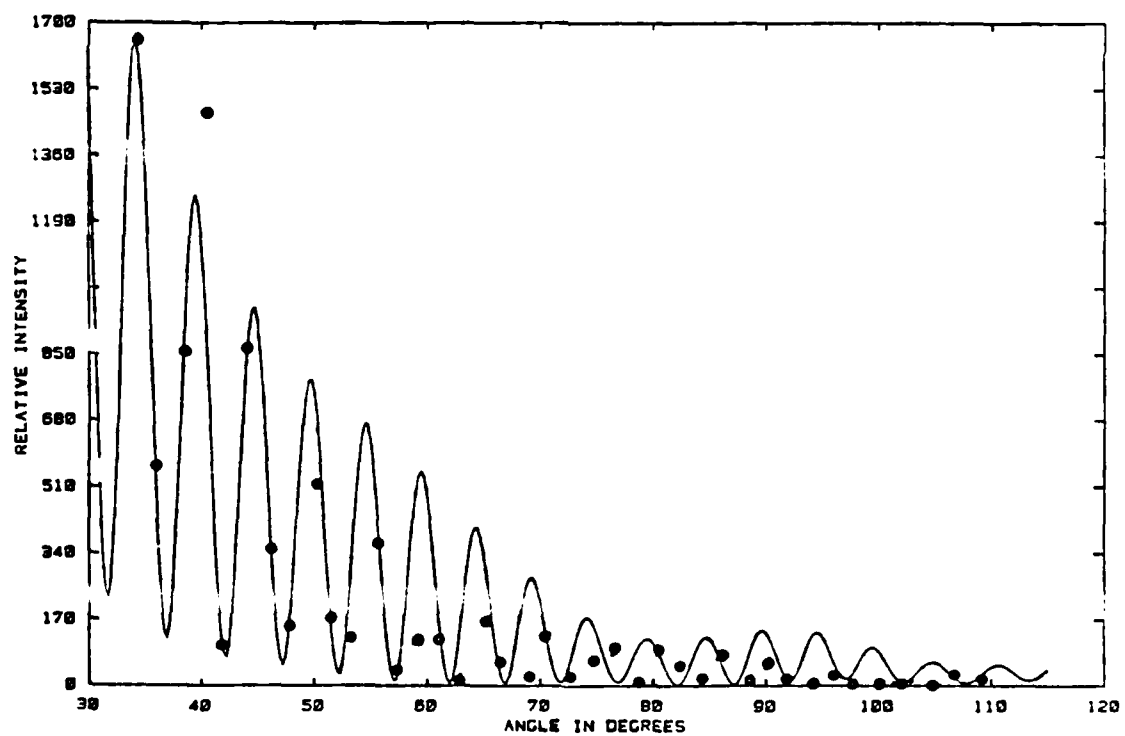

Figure 50.   Mie theory (———) for α = 40.6 and m = 1.5177 - i0.0045
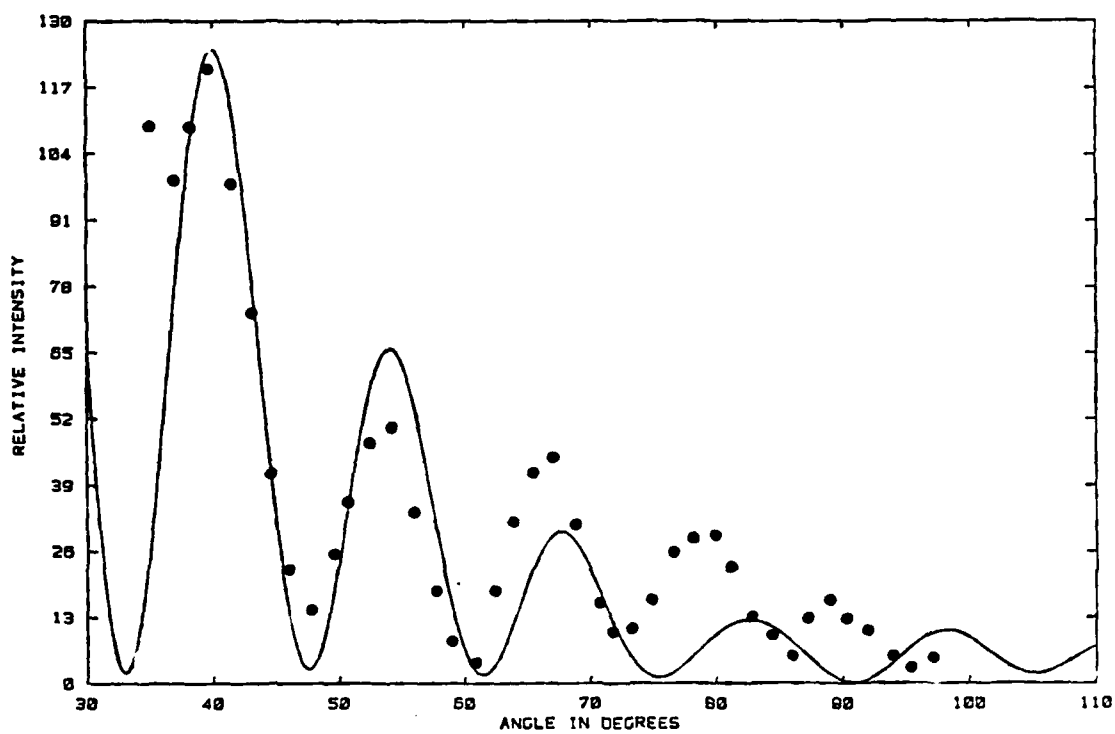
compared with light-scattering data (•) for Sample 138B

52

Figure 51.   Mie theory (———) for α = 13.7 and m = 1.3948 - i0.0169 compared with light-scattering data (·) for Sample 138C.

53

54

DISTRIBUTION LIST

DEPARTMENT OF DEFENSE

DEFENSE INTELLIGENCE AGENCY
ATTN: RTS-2A (TECH LIB)
ATTN: RTS-2B

DEFENSE NUCLEAR AGENCY
ATTN: SPAS G ULLRICH
4 CYS ATTN: STTI-CA

DEFENSE TECHNICAL INFORMATION CENTER
12 CYS ATTN: DD

FIELD COMMAND
ATTN: FCTT
ATTN: FCTT W SUMMA
ATTN: FCTXE

JOINT STRAT TGT PLANNING STAFF
ATTN: JLKS
ATTN: JPTM
ATTN: JPTP

UNDER SECYS OF DEF FOR RSCH & ENGRG
ATTN: STRAT & SPACE SYS(OS)
ATTN: STRAT & THEATER NUC FOR. F VAJDA

DEPARTMENT OF THE ARMY

HARRY DIAMOND LABORATORIES
ATTN: SCHLD-NW-P
ATTN: SLCIS-IM-TL (81100) (TECH LIB)

U S ARMY BALLISTIC RESEARCH LAB
ATTN: SLCBR-SS-T (TECH LIB)

U S ARMY CORPS OF ENGINEERS
ATTN: DAEN-ECE-T

U S ARMY ENGINEER CTR & FT BELVOIR
ATTN: TECHNICAL LIBRARY

U S ARMY ENGINEER DIV HUNTSVILLE
ATTN: HNDEN-FO

U S ARMY NUCLEAR & CHEMICAL AGENCY
ATTN: LIBRARY
ATTN: MONA-NU MR LONG

U S ARMY STRATEGIC DEFENSE CMD
ATTN: DASD-H-SAV R C WEBB

U S ARMY STRATEGIC DEFENSE COMMAND
ATTN: ATC-T

DEPARTMENT OF THE NAVY

NAVAL RESEARCH LABORATORY
ATTN: CODE 2627 (TECH LIB)
ATTN: CODE 4040 D BOOK
ATTN: CODE 4040 J BORIS

NAVAL SURFACE WEAPONS CENTER
ATTN: CODE R44 H GLAZ
ATTN: CODE X211 (TECH LIB)

NAVAL SURFACE WEAPONS CENTER
ATTN: TECH LIBRARY & INFO SVCS BR

OBRIEN (DD 975)
ATTN: COMMANDING OFFICER

DEPARTMENT OF THE AIR FORCE

AIR FORCE CTR FOR STUDIES & ANALYSIS
ATTN: AFCSA/SAMI (R GRIFFIN)

AIR FORCE INSTITUTE OF TECHNOLOGY
ATTN: LIBRARY/AFIT/LDEE

AIR FORCE WEAPONS LABORATORY. AFSC
ATTN: NTED-A
ATTN: SUL

BALLISTIC MISSILE OFFICE/DAA
ATTN: ENSN
ATTN: MYED D GAGE

STRATEGIC AIR COMMAND/NRI-STINFO
ATTN: NRI/STINFO

STRATEGIC AIR COMMAND
ATTN: XPFS

DEPARTMENT OF ENERGY

LOS ALAMOS NATIONAL LABORATORY
ATTN: C F KELLER
ATTN: M T SANDFORD
ATTN: R WHITAKER

SANDIA NATIONAL LABORATORIES
ATTN: DIV 7111 J W REED
ATTN: J R BANNISTER 7111
ATTN: ORG 7112 A CHABAI

CENTRAL INTELLIGENCE AGENCY
ATTN: OSWR/NED

DEPARTMENT OF DEFENSE CONTRACTORS

ACUREX CORP
ATTN: C WOLF

AEROSPACE CORP
ATTN: H MIRELS
ATTN: LIBRARY ACQUISITION M1/199

APPLIED RESEARCH ASSOCIATES, INC
ATTN: N HIGGINS

APPLIED RESEARCH ASSOCIATES, INC
ATTN: D PIEPENBURG

BOEING CO
ATTN: M/S 13-13 S STRACK

CALIFORNIA RESEARCH & TECHNOLOGY, INC
ATTN: K KREYENHAGEN
ATTN: LIBRARY

CALIFORNIA RESEARCH & TECHNOLOGY, INC
ATTN: F SAUER

CARPENTER RESEARCH CORP
ATTN: H J CARPENTER

DENVER, UNIVERSITY OF
ATTN: J WISOTSKI

H & H CONSULTANTS, INC
ATTN: J HALTIWANGER
ATTN: W HALL

H-TECH LABS, INC
ATTN: B HARTENBAUM

KAMAN SCIENCES CORP
ATTN: R RUETENIK

KAMAN TEMPO
ATTN: DASIAC

KAMAN TEMPO
ATTN: DASIAC

MCDONNELL DOUGLAS CORP
ATTN: H HERDMAN
ATTN: R HALPRIN

MISSION RESEARCH CORP
ATTN: C LONGMIRE

NEW MEXICO ENGINEERING RESEARCH INSTITUTE
2 CYS ATTN: D CALHOUN
ATTN: G LEIGH

NEW MEXICO, UNIVERSITY OF
ATTN: J KOVARNA

NICHOLS RESEARCH CORP, INC
ATTN: R BYRN

PACIFIC-SIERRA RESEARCH CORP
ATTN: H BRODE, CHAIRMAN SAGE

PACIFIC-SIERRA RESEARCH CORP
ATTN: D GORMLEY

PACIFICA TECHNOLOGY
ATTN: R ALLEN
ATTN: TECH LIBRARY

PATEL ENTERPRISES, INC
ATTN: M PATEL

PHYSICAL RESEARCH, INC
ATTN: R DELIBERIS
ATTN: W MENDES

PHYSICS INTERNATIONAL CO
ATTN: H W WAMPLER

R & D ASSOCIATES
ATTN: A KUHL
ATTN: TECHNICAL INFORMATION CENTER

RAND CORP
ATTN: B BENNETT

S-CUBED
ATTN: C DISMUKES
ATTN: J BARTHEL
ATTN: K PYATT
ATTN: LIBRARY

S-CUBED
ATTN: C NEEDHAM

SCIENCE & ENGRG ASSOC., INC
ATTN: B CHAMBERS

SCIENCE APPLICATIONS INTL CORP
ATTN: H WILSON
ATTN: R SCHLAUG
ATTN: TECHNICAL LIBRARY

SCIENCE APPLICATIONS INTL CORP
ATTN: J COCKAYNE
ATTN: W LAYSON

SCIENCE APPLICATIONS INTL CORP
ATTN: G BINNINGER

DEPT OF DEFENSE CONTRACTORS (CONTINUED)

SRI INTERNATIONAL
    ATTN: J COLTON

TELEDYNE BROWN ENGINEERING
    ATTN: D ORMOND
    ATTN: F LEOPARD

TRW ELECTRONICS & DEFENSE SECTOR
    ATTN: N LIPNER
    ATTN: TECH INFO CTR,DOC ACQ

TRW ELECTRONICS & DEFENSE SECTOR
    ATTN: E WONG
    ATTN: G HULCHER
    ATTN: P DAI

UNIVERSITY OF WASHINGTON
2 CYS ATTN: E DAVIS
2 CYS ATTN: R PERIASAMY

WEIDLINGER ASSOC, CONSULTING ENGRG
    ATTN: I SANDLER

END

DTIC

9 — 86